

IMAGE-BASED ROAD PAVEMENT MACROTEXTURE DETERMINATION

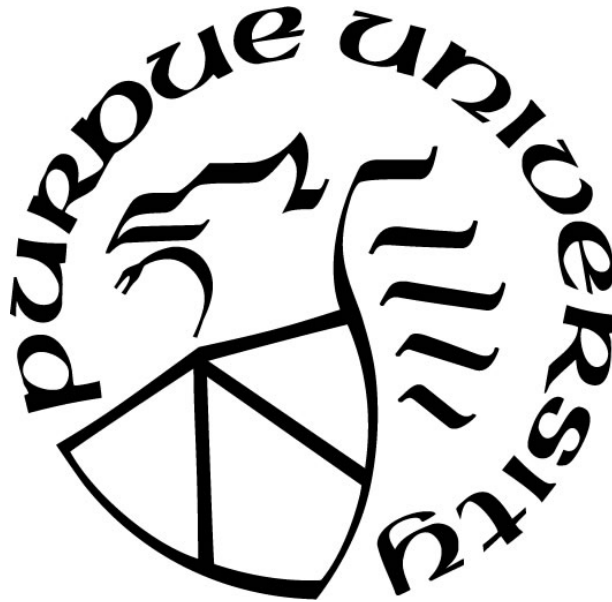
by
Xiangxi Tian

A Thesis

Submitted to the Faculty of Purdue University

In Partial Fulfillment of the Requirements for the degree of

Master of Science in Civil Engineering



Lyles School of Civil Engineering

West Lafayette, Indiana

December 2019

THE PURDUE UNIVERSITY GRADUATE SCHOOL
STATEMENT OF COMMITTEE APPROVAL

Dr. Jie Shan, Chair

Lyles School of Civil Engineering

Dr. James S. Bethel

Lyles School of Civil Engineering

Dr. Antonio Bobet

Lyles School of Civil Engineering

Approved by:

Dr. Dulcy Abraham

Chair, Burke Graduate Program, Lyles School of Civil Engineering

ACKNOWLEDGMENTS

Foremost, I would like to express my sincere gratitude to my advisor Prof. Jie Shan for the continuous support of my study and research, and for his patience, motivation, enthusiasm, and immense knowledge. His guidance helped me in all the time of research and writing of this thesis. Besides my advisor, I would like to thank the rest of my advisory committee: Prof. James Bethel and Prof. Antonio Bobet for their kindness, encouragement, and insightful comments. My sincere thanks also go to Dr. Shuo Li at the Division of Research and Development of INDOT, who gave me access to this research and research facilities. Without his precious support it would not be possible to finish my degree. I am extremely thankful for Dr. Oguz Gungor, Dr. Yong Xu, Fulu Wei, Ce Wang, Yuchi Ma, Zhixin Li, and Xiaoyi Peng for helping collecting research data and sharing expertise. I am also grateful to INLTAP for providing me with research assistant opportunity and encouragement. The work experience I have gained and skills I have developed from this research assistant opportunity are valuable. I would like to express my special thanks to Laura Slusher, my manager at INLTAP. She not only mentored me technically, but also helped me to build up confidence and gave me immense encouragement. Last but not the least, I would like to thank my parents for supporting me spiritually throughout writing this thesis and for their unceasing encouragement and attention.

TABLE OF CONTENTS

LIST OF TABLES	6
LIST OF FIGURES	7
LIST OF SYMBOLS	9
ABSTRACT.....	10
1. INTRODUCTION	11
1.1 Background.....	11
1.2 Objectives	13
1.3 Previous work	14
1.4 Structure of the thesis.....	18
2. THEORY AND METHODOLOGY	19
2.1 Macrottexture metrics	19
2.1.1 Mean profile depth (MPD)	19
2.1.2 RMS height (σ_h)	20
2.1.3 Aggregate loss percentage	21
2.2 Methodology	23
2.2.1 Keypoint generation.....	23
2.2.2 Bundle adjustment	25
2.2.3 Dense point cloud generation	26
2.2.4 Image-based MPD calculation.....	27
2.2.5 RMS height calculation	28
2.2.6 Point cloud segmentation.....	28
2.2.7 Calculation for the volume of remaining aggregate	30
3. EQUIPMENT AND DATA COLLECTION	32
3.1 Equipment.....	32
3.2 Data collection procedure	35
3.3 Sites of data collection	36
3.3.1 INDOT test site.....	36
3.3.2 Road sites.....	37
3.3.3 Sample plates for aggregate loss analysis.....	38

3.4	Quality of the 3D models from images	39
4.	RESULTS AND EVALUATION	45
4.1	MPD results and evaluation	45
4.1.1	MPD results for test site at INDOT	45
4.1.2	MPD results for road sites	47
4.1.3	MPD for any direction	49
4.1.4	Summary	50
4.2	Evaluation of Aggregate Loss	50
4.2.1	Evaluate aggregate loss via RMS height	50
4.2.2	Evaluate aggregate loss via volume	53
4.2.3	Summary	58
5.	CONCLUSION	59
	REFERENCES	61

LIST OF TABLES

Table 2.1. Spacing between adjacent profiles obtained from LTS.	28
Table 3.1. Characteristics of LTS model 9400	32
Table 3.2. Characteristics of iPhone 8 Plus camera.....	33
Table 3.3. Summary on the measurements of the GCPs on control frame A.	34
Table 3.4. Summary of data collected at the INDOT test site spots.....	36
Table 3.5. Summary of data collected at the test spots on State Roads.....	38
Table 3.6. Average RMS residuals of GCPs used by two control frames.....	41
Table 3.7. Summary of the residuals of 3D models.....	41
Table 3.8. Characteristics of the residual distribution in Figure 3.7.....	41
Table 4.1. MPD from LTS and images for the INDOT test site.....	46
Table 4.2. Summary of the MPD of three road sites by LTS and images.	47
Table 4.3. MPD from LTS and image-based methods for SR 32 about 8 months after construction.	48
Table 4.4. MPD from LTS and image-based methods for SR 446 about 5 months after construction.	48
Table 4.5. MPD from the LTS and image-based methods for SR 205 about 5 months after construction.	49
Table 4.6. Calculated MPD of sample plates with different aggregate loss percentage.....	51
Table 4.7. Calculated RMS height of sample plates with different aggregate loss percentage....	52
Table 4.8. Residuals of exponential fitting for aggregate loss percentage on RMS height.....	53
Table 4.9. Optimal number of classes and volume of aggregate remained on each sample plate.	54
Table 4.10. Residuals of exponential fitting for aggregate loss percentage on volume.	57
Table 4.11. Summary of the evaluation of two exponential fitting models.....	58

LIST OF FIGURES

Figure 1.1. Illustration of concepts of microtexture and macrotexture. (Flintsch et al. 2003)	12
Figure 1.2. Sand patch method (left) and outflow meter (right) (Aktas et al. 2011) for macrotexture calculation.	15
Figure 2.1. Procedure of MSD computation. (ASTM 2009)	20
Figure 2.2. Illustration of an intact pavement surface (left) and a pavement surface with serious aggregate loss (right).....	23
Figure 2.3. Keypoints detection conducted by Agisoft Metashape: (a) original image, and (b) 295,408 keypoints detected for this image.	25
Figure 2.4. Keypoint matching between two images.....	25
Figure 2.5. Output of bundle adjustment.	26
Figure 2.6. Sparse point cloud (left) and the dense point cloud (right).	27
Figure 2.7. Example of a 3D model of pavement (100 mm × 90 mm) (left) and its height deviation segmentation through Otsu’s method (right, mm).	30
Figure 2.8. Three scenarios for calculating the volume of a grid.	31
Figure 3.1. LTS model 9400 (left); iPhone 8 plus (right).	32
Figure 3.2. Two control frames made for image collection. (a) Control frame A used for collecting images for MPD calculation. (b) Control frame B used for collecting images for aggregate loss analysis.....	34
Figure 3.3. Process of data collection on road for MPD measurement.	35
Figure 3.4. Testing site at INDOT.	36
Figure 3.5. Road sites on SR 32 (left), SR 446 (middle) and SR 205 (right).	38
Figure 3.6. Seven sample plates (150 mm×150 mm) for aggregate loss analysis.	39
Figure 3.7. Residual distribution of tie points in X direction (left) and Y direction (right).	41
Figure 3.8. Six 3D models for MPD measurement at INDOT test site.	42
Figure 3.9. Three 3D models for MPD measurement at SR 32.....	42
Figure 3.10. Ten 3D models for MPD measurement at SR 446.....	43
Figure 3.11. Twelve 3D models for MPD measurement at SR 205.	44
Figure 3.12. Seven 3D models of sample plates for aggregate loss analysis.....	44
Figure 4.1. Comparison between MPDs of 10 profiles for spot 2 (left), spot 5 (middle) and spot 6 (right) at INDOT.....	46

Figure 4.2. MPD for any direction for six testing spots at INDOT.	50
Figure 4.3. Illustration of the relationship between aggregate loss percentage and RMS height using (a) linear regression and (b) exponential fitting.	52
Figure 4.4. Effectiveness of thresholding vs. number of classes for seven sample plates.....	54
Figure 4.5. Comparison between original 3D model and the thresholding results of Otsu’s method for seven sample plates.	55
Figure 4.6. Illustration of the relationship between aggregate loss percentage and volume of remaining aggregate using (a) linear regression and (b) exponential fitting.	57

LIST OF SYMBOLS

Across road direction	x -axis
Along road direction	y -axis
Perpendicular to road surface	z -axis
Dimension of study spot	$x \in [x_a, x_b], y \in [y_a, y_b]$
Profile (height deviation) of the pavement	$z = h(x, y)$
Mean profile depth	MPD
Aggregate loss percentage	a
Weight of remaining aggregate on the road	W
Weight of remaining aggregate without loss	W_0
Root mean square height	σ_h
Volume of remaining aggregate on the road	V
Volume of remaining aggregate without loss	V_0

ABSTRACT

Pavement macrotexture contributes greatly to road surface friction, which in turn plays a significant role in reducing road incidents. Conventional methods for macrotexture measurement techniques (e.g., the sand patch method, the outflow method, and laser measuring) are either expensive, time-consuming, or of poor repeatability. This thesis aims to develop and evaluate affordable and convenient alternative approaches to determine pavement macrotexture. The proposed solution is based on multi-view smartphone images collected in situ over the pavement. Computer vision techniques are then applied to create high resolution three-dimensional (3D) models of the pavement. The thesis develops the analytics to determine two primary macrotexture metrics: mean profile depth and aggregation loss. Experiments with 790 images over 25 spots of three State Roads and 6 spots of the INDOT test site demonstrated that the image-based method can yield reliable results comparable to conventional laser texture scanner results. Moreover, based on experiments with 280 images over 7 sample plates with different aggregate loss percentage, the newly developed analytics were proven to enable estimation of the aggregation loss, which is largely compromised in the laser scanning technique and conventional MPD calculation approach. The root mean square height based on the captured images was verified in this thesis as a more comprehensive metric for macrotexture evaluation. It is expected that the developed approach and analytics can be adopted for practical use at a large scale.

1. INTRODUCTION

1.1 Background

The quality properties of road pavements have direct and significant impacts on road safety. According to *Indiana Crash Facts 2017*, about 200,000 vehicle crashes occurred in Indiana every year from 2013 through 2017, of which about 34,000 accidents resulted in injuries and 755 accidents caused fatalities. Ten percent of these accidents were further attributed to insufficient surface friction on road curves.

It is essential to provide adequate friction and drainage to reduce the possibility of accidents on roads; and these two properties are mainly determined by pavement surface textures. Pavement surface texture, which can be defined as the deviation of a pavement surface from a true planar surface (Li et al. 2016), directly affects the various parameters resulting from tire-road interactions such as friction, tire noise, skid resistance, tire wear, rolling resistance, splash and spray, traffic vibration, etc. (Ejsmont et al. 2017, Das et al. 2015, Yaacob et al. 2014). It was suggested in the 1987 Permanent International Association of Road Congresses (PIARC), depending on the amplitude and wavelength of a feature, to divide the pavement surface characteristics (the geometric profile of a road in the vertical plane) in four categories: roughness (unevenness), megatexture, macrotexture, and microtexture (Dong et al. 2019, Bitelli et al. 2012, Dunford 2013).

Roughness refers to the unevenness, potholes, and large cracks on road surfaces that are larger than a tire footprint (Dong et al. 2019, Bitelli et al. 2012, Dunford 2013). Irregularities in this size correspond to wavelengths ranging from 0.5 m to 50 m, which further correspond to a range of vertical dimensions varying from 1 mm to 200 mm (Dong et al. 2019, Das et al. 2015, Dunford 2013). Roughness can affect a vehicle's dynamics, speed, ride quality, drainage, fuel consumption, and tire wear (Abulizi et al. 2016, Douangphachanh et al. 2013, Dunford 2013, Paterson 1986) and can even cause traffic accidents by leading to a vehicle's loss of contact with the pavement surface. To determine pavement roughness, repeatable profile measurements, which are often called profiling, are completed. On the other hand, megatexture is associated with deviations in wavelengths from 50 mm to 500 mm and vertical amplitudes ranging from 0.1 mm to 50 mm (Dong et al. 2019, Dunford 2013). Texture of this size is mainly caused by poor

construction practices or surface deterioration. This level of texture causes vibrations in tire walls, resulting in vehicle noise and some external noise.

Macrotexture and microtexture refer to the relatively small pavement surface irregularities that primarily affect friction and skid resistance, which are illustrated in Figure 1.1. Macrotexture refers to the changes in wavelengths ranging from 0.5 mm to 50 mm horizontally and variations ranging from 0.1 mm to 20 mm vertically (Dong et al. 2019). However, microtexture, which corresponds to wavelengths less than 0.5 mm horizontally and vertical amplitudes up to 0.2 mm, is related to the roughness of the individual stone elements used in the surface layer and to the natural mineral aggregate (Bitelli et al. 2012). The microtexture of the road surface affects skid resistance and is responsible for stopping on dry pavements. Good microtexture also provides adequate stopping on wet pavements if the vehicle speed is less than 50 mph (80 kph) and the surface of the road is not flooded. However, if the vehicle travels at speeds of 50 mph (80 kph) or greater, the friction of the pavement surface in wet circumstance is directly related to the macrotexture instead (Snyder 2006). Good macrotexture provides rapid drainage of water during rain events between the tire and the pavement, thus allowing better tire contact with the pavement to improve frictional resistance and prevent hydroplaning (Babu et al. 2019, Snyder 2006).

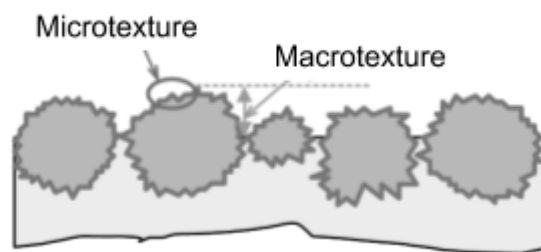


Figure 1.1. Illustration of concepts of microtexture and macrotexture. (Flintsch et al. 2003)

One other aspect of the pavement that should be considered for road quality is the failure mode. For normal pavement roads, there are many visible failure modes (e.g., aggregate polishing, bleeding, and aggregate loss (Gransberg 2008). A literature review and agency survey conducted by Gransberg and James (2005) indicated that aggregate loss is one of the most common visible chip seal surface failure modes. The theory of aggregate loss is sophisticated and includes many factors, but the specific influence of each factor is still undecided (Miradi 2004, Adams 2017). These factors include low binder application rate, dirty or dusty aggregate, cold weather, delayed

aggregate application, and traffic patterns (Adams 2017). Despite the fact that aggregate loss is an inevitable problem, excessive aggregate loss may cause serious safety concerns (Massahi et al. 2018). For example, flying aggregate fragments can threaten the safety of vehicles and pedestrians (Massahi et al. 2018), and water tends to accumulate at the aggregate loss area, which can lead to a significant reduction in surface friction (Baqersad et al. 2016, Massahi et al. 2018). Therefore, it is important to quantify the aggregate loss.

1.2 Objectives

The objectives of this thesis are to explore new technologies and methods to determine pavement macrotexture. The conventional methods for determining road macrotexture include the sand patch method, the outflow method, and laser profiling. The sand patch method is operator-dependent and the test results have poor repeatability (Sengoz et al. 2012). Other problems with the sand patch method include that on surfaces with very deep textures it is very easy to overestimate the texture depth (Fisco et al. 2014), and accurate sand patch testing cannot be done when the road surface is sticky or wet (Praticò et al. 2015). As is the case with the sand patch method, the outflow method also is labor-intensive and time-consuming, and the reliability of the results depends largely on the operator (Wang et al. 2011). Laser-based linear profiling devices have been shown to improve testing efficiency to a great degree (Fisco et al. 2014, Flintsch et al. 2003), but this method is not cost-effective because of the relatively high cost of the laser equipment and the need for routine calibration (Wang et al. 2011). Moreover, its high cost also restricts its use over large areas for multi-division transportation agencies.

Due to the drawbacks and shortcoming for all of the above existing methods and techniques, the transportation industry is in need of an effective, low-cost approach to measuring pavement quality. To meet this need, this thesis investigates and introduces a low-cost, ubiquitous image-based sensing technique for pavement macrotexture measurement. The novel approach presented here uses smartphone images collected onsite to generate accurate and detailed three-dimensional (3D) pavement models. Then, analytics also developed in this thesis are used to determine and analyze the pavement macrotexture on the road. Based on the analytics and using high resolution 3D pavement models from the structure from motion (SfM) technique, this thesis confirms that the developed image-based macrotexture measurement approach is convenient, cost-effective, and

comparable to the conventional methods. Moreover, the limitations of the current approach are addressed and alternative analytics are developed to determine the aggregate loss of pavement.

1.3 Previous work

Although both microtexture and macrotexture contribute to pavement friction, there is currently no practical procedure for direct measurement of the microtexture profile in traffic (Dong et al. 2019, Henry 2000). The PIARC Model for the International Friction Index (IFI) avoids the need for measuring microtexture if macrotexture measures are available. A measurement at any slip speed, together with the macrotexture parameter, determines the friction as a function of the slip speed (Henry 2000). The typical parameter to describe pavement macrotexture is the mean profile depth (MPD) or the mean texture depth (MTD). MPD is linear related to MTD and is usually converted to MTD when comparing different macrotexture calculation methods (Fisco et al. 2014, Henry 2000). There are several conventional macrotexture calculation methods.

The traditional macrotexture measuring method is referred to as the sand patch method, which is commonly used as the reference method when comparing the results obtained with other methods. The sand patch method consists of spreading a specified volume of sand (or glass spheres) on the pavement in a circular motion with a spreading tool; and the area of this roughly circular patch of sand is then calculated by using the average of four equally spaced diameters (Fisco et al. 2014, Henry 2000), see Figure 1.2. The volume divided by the area is reported as the MTD. Although the sand patch method is currently used as a reference ground truth throughout the world, it is commonly known that it is an operator-dependent method and its test results have poor repeatability (Yaacob et al. 2014, Sengoz et al. 2012). Another problem with the sand patch method is that on surfaces with very deep textures, the glass spheres tend to flow under the sides of the fixture and subsequently the texture depth is overestimated (Fisco et al. 2014). Also, accurate sand patch testing cannot be done when the road surface is sticky or wet (Praticò et al. 2015).

Another classical method is the outflow method, which establishes the relationship between the macrotexture and the time of discharge of water in a receptacle. The outflow meter is a transparent vertical cylinder that rests on a rubber bottom placed on the pavement (Aktas et al. 2011), see Figure 1.2. A valve at the bottom of the cylinder is closed and the cylinder is filled with water. The valve is then opened and the time required for the water level in the cylinder to drop from the upper reference line to the lower reference line is recorded. Very short outflow times

indicate rough surface textures and long outflow times indicate smooth surfaces (Aktas et al. 2011). Since outflow time is highly correlated with MTD, the outflow method is used to indirectly estimate pavement texture. As a labor-intensive and time-consuming process, the reliability of the outflow method results, like the sand patch method, largely depends on the operator (Wang et al. 2011).

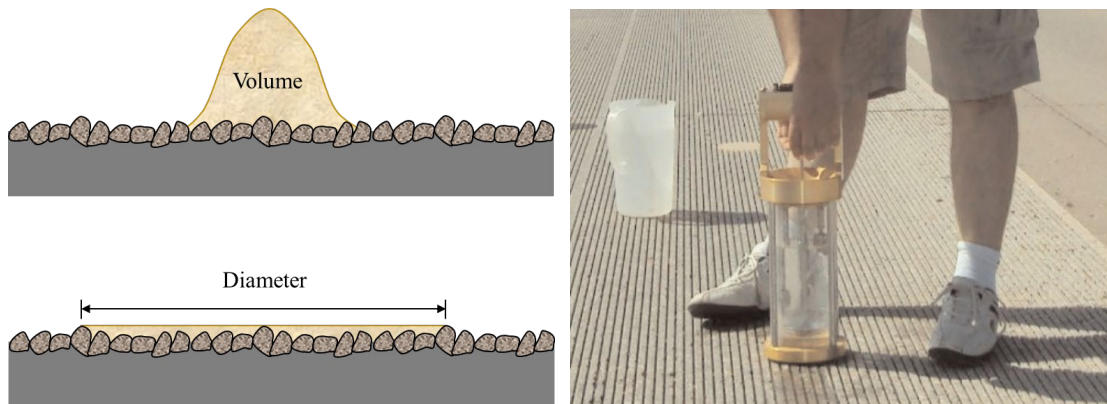


Figure 1.2. Sand patch method (left) and outflow meter (right) (Aktas et al. 2011) for macrotexture calculation.

More recently, macrotexture measurements have been performed using laser measurement devices. These devices can obtain depth information by making distance measurements on the road surface at certain intervals along a line. This depth information is used to calculate the MPD (Fisco et al. 2014, Yaacob et al. 2014, Cigada et al. 2010, Bitelli et al. 2012), which is standardized in American Society for Testing and Materials (ASTM) E1845, for expressing the macrotexture properties of pavement. One of the laser measurement devices used to determine the texture of a pavement is the circular track or texture meter (CTMeter) (Fisco et al. 2014). The CTMeter uses a laser that rotates on a circumference to measure the pavement profile in a circle that can vary in size. In 2014 Fisco et al. used a CTMeter with a 284 mm diameter circle track to measure the texture with a sampling interval of approximately 0.9 mm. While laser profilers can be static measuring devices, there are also vehicle-mounted versions that collect laser measurements at traffic speeds. The CTMeter is relatively expensive, can only measure macrotexture with longer wave lengths, and has a low percentage of repeatability and reproducibility. Furthermore, it is difficult to evaluate grooved surfaces with the CTMeter since it measures texture data in a circular ring (Wang et al. 2011, Byrum et al. 2010). Laser-based devices measuring linear profiles, which are known as laser texture scanners, improve the testing efficiency to a great degree while

maintaining good correlation with the sand patch method or the CTMeter (Fisco et al. 2014, Flintsch et al. 2003). However, these systems are very expensive (Wang et al. 2011); and as is the case with the sand patch method, the accuracy of the laser-based devices decreases on wet, shiny, and sticky surfaces. Since the laser can only measures a 2D profile, another significant defect of laser-based measurement is that it is a 2D estimation of the pavement, which is clearly a 3D surface.

As an alternative to the methods described above, there also have been studies using image-based techniques to characterize macrotexture properties. In 2011, El Gendy et al. used a two-camera photometric stereo system developed by Flintsch et al. in 2008 to reconstruct the 3D texture of pavement. This stereo-vision system (SVS) can recover the pavement surface height by capturing two images of the same scene using two cameras separated by a small baseline distance with the location of a point on the pavement derived through triangulation in stereo-imaging (Gendy et al. 2011). In order to reduce variability, the SVS utilizes an enclosure to isolate the scene from ambient lighting (Gendy et al. 2011). The system is large in size, which restricts its portability and makes it inconvenient for measurement. In 2018, Kogbara et al., using a handheld Canon™ 6D EOS digital full frame single lens reflex camera, captured twelve images for each study spot and generated dense point clouds of pavement surfaces with 3DF Zephyr Pro v3.142 proprietary software (3DFlow, Verona, Italy), upon which the surface texture parameters were calculated (Kogbara et al. 2018). Although the dense point cloud was generated, the quality of it was not discussed in their work.

However, no studies were found in the reviewed literature using multiple images collected by mobile phone cameras, which is much more convenient, flexible, and affordable. Considering the widespread usage of smartphones, using a mobile phone camera to measure the pavement surface would be a much cheaper and more convenient approach to determine the pavement macrotexture.

In traditional photogrammetry, overlapping images collected from different viewpoints are used to reconstruct 3D scene geometry. To calculate the 3D position of a point in object space, the exterior orientation (position and orientation of the camera when the image was collected) and the interior orientation (location of the principle point and the focal length of the camera) parameters are needed. Exterior orientation parameters establish the relationship between the object space and the image plane while the interior orientation parameters establish the relationship between the image plane and the projection center of the camera. In most cases, the exterior

orientation parameters are computed from the ground control points (GCP) and tie points (TP). Once the interior and exterior orientation parameters are determined, a 3D representation of the object space covered by the overlap area can be derived through relative and absolute orientation procedures. On the other hand, the bundle block adjustment technique, which was first introduced by Brown (1971), constructs a rigorous mathematical relationship between the image and the object space. By utilizing collinearity equations, the image coordinates of the selected features can be related to the corresponding ground coordinates and interior and exterior orientation parameters. Finally, simultaneous least squares adjustment solves the ground coordinates of the tie points and the exterior orientation parameters.

The Structure from Motion (SfM) method, first proposed in 1979 by S. Ullman, was originally based on the bundle adjustment technique (Ullman 1979). SfM uses images collected from different viewpoints but differs from traditional photogrammetry in that it automatically estimates the interior and exterior orientation parameters without using any GCPs established on the ground and seen in photos (Micheletti et al. 2014, Westoby et al. 2012). This method became possible by the emergence of algorithms such as SIFT (Lowe 1999), which were developed in the machine vision area, and are able to compute interior and exterior orientation parameters without any control point by matching the correspondence points in the images obtained from different viewpoints. However, SfM requires a much larger overlap in sequentially-captured images, just as in the case where one uses a moving sensor to create the 3D geometry of a structure, thus justifying method's SfM name (Micheletti et al. 2014).

As for the measurement of aggregate loss, Li et al. proposed an approach in 2012 to measure surface macrotexture that could be related to aggregate loss since the excessive aggregate loss can cause catastrophic decreases in the macrotexture depth (Li et al. 2012). However, this approach is difficult to conduct due to the fact that pavement macrotexture is commonly measured using laser devices nowadays. As mentioned above, laser devices provide a 2-D solution for a 3D surface and therefore cannot provide a complete representation of the pavement macrotexture.

Based on the above literature review, this thesis proposes a novel approach to determine pavement macrotexture using mobile phones to collect images on site with large overlap and redundancy. The SfM technique is utilized in this approach to create accurate and dense 3D pavement models with Agisoft Metashape software. Based on the developed analytics, the MPD and the aggregate loss can be determined from the created 3D pavement model.

1.4 Structure of the thesis

This remainder of this thesis proceeds as follows. Chapter 2 presents the definitions and calculations for several metrics and the major methods used for 3D model generation and analysis. Also in Chapter 2, SfM is introduced as the method for 3D reconstruction from multi-view images as well as Otsu's method for separating the remaining aggregate from the ground surface. Chapter 3 discusses the equipment, location, and sample plates prepared for data collection; and the measuring mechanism of the laser texture scanner is described in detail as well as the quality of the 3D model generated from the images. One of the data collection location is the Indiana Department of Transportation (INDOT), and the others are three state roads which are SR 32, SR 446, and SR 205. Chapter 4 first presents the results of the calculated MPD, a comparison between the MPD results of the laser texture scanner and the 3D models from the images, and a summary of the results. Two approaches for aggregate loss evaluation are also introduced in Chapter 4. In Chapter 5, major results and contributions of this thesis are described along with possible future improvements.

2. THEORY AND METHODOLOGY

This chapter first introduces the metrics for macrotexture measurement including MPD and RMS height, and the aggregate loss percentage is proposed to evaluate aggregate loss. Then, the several methods implemented in this thesis are discussed for 3D model generation and analysis, which includes SfM, bundle adjustment, MVS, and Otsu's method. Moreover, the calculations for the image-based method including image-based MPD calculation, RMS height calculation, point cloud segmentation, and the volume calculation are presented in detail.

2.1 Macrotexture metrics

This section will describe the various metrics for pavement macrotexture. Depending on the nature of the measurement, different definitions for pavement macrotexture may be used. The classical mean profile depth (MPD) is first introduced followed by the mean segment depth (MSD) and then a metric based on plane fitting. The concept of aggregate loss is also described.

2.1.1 Mean profile depth (MPD)

According to ASTM E1845-09 (ASTM 2009), MPD is the average of all the mean segment depths for all the segments of a profile, while the mean segment depth (MSD) is the average value of peak level (1st) and peak level (2nd) having a given baseline, as shown in Figure 2.1 (ASTM 2009).

Suppose the profile of a pavement texture is denoted by

$$z = h(x), \quad x \in [x_a, x_b] \quad (2-1)$$

The average level for the profile is denoted as Equation 2-2 and its coefficients are determined via Equation 2-3.

$$a_1x + b_1z + c_1 = 0, \quad x \in [x_a, x_b] \quad (2-2)$$

$$\underset{a_1, b_1, c_1}{\operatorname{argmin}} \sum_{i=1}^n \left(h(x_i) + \frac{a_1x_i + c_1}{b_1} \right)^2 \quad (2-3)$$

Equation 2-4 (ASTM 2009) is the calculation equation of MSD. It is noted that the baseline is 100±2 mm long. According Equation 2-2, the calculation of MSD can be further determined via

Equation 2-5. Suppose the number of profiles is m , then MPD is calculated by averaging the MSDs of all profile, see Equation 2-6.

$$MSD = \frac{Peak\ level\ (1^{st}) + Peak\ level\ (2^{nd})}{2} \quad (2-4)$$

$$MSD = \frac{1}{2} \times \left(\max \frac{|a_1 x_j + b_1 h(x_j) + c_1|}{\sqrt{a_1^2 + b_1^2}} + \max \frac{|a_1 x_k + b_1 h(x_k) + c_1|}{\sqrt{a_1^2 + b_1^2}} \right) \quad (2-5)$$

$$x_j \in \left[x_a, \frac{(x_b - x_a)}{2} \right], x_k \in \left[\frac{(x_b - x_a)}{2}, x_b \right]$$

$$MPD = \frac{1}{m} \sum_{i=1}^m MSD_i \quad (2-6)$$

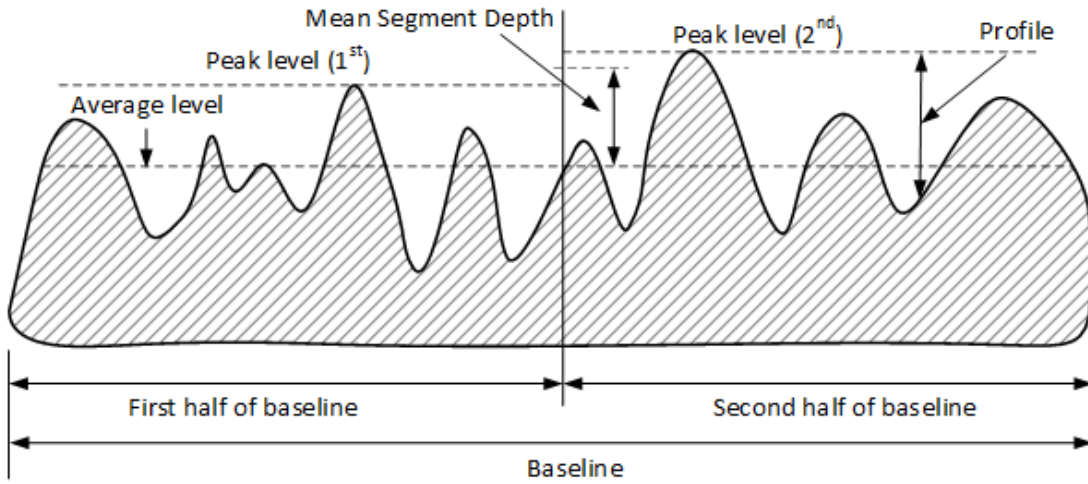


Figure 2.1. Procedure of MSD computation. (ASTM 2009)

2.1.2 RMS height (σ_h)

We propose this metric as an alternative and supplement to the classical MPD. It will be shown later that this metric is advantageous when working with 3D pavement models. It is a 3D generalization of the 2D MPD concept.

Suppose the pavement surface is described by

$$z = f(x, y), \quad x \in [x_a, x_b], y \in [y_a, y_b] \quad (2-7)$$

and the mean surface plane of pavement is represented by Equation 2-8. The coefficients of the mean surface plane can be determined using least squares fitting, see Equation 2-9.

$$a_2 x + b_2 y + c_2 z + d_2 = 0, \quad x \in [x_a, x_b], y \in [y_a, y_b] \quad (2-8)$$

$$\operatorname{argmin}_{a_2, b_2, c_2, d_2} \sum_{i=1}^n \sum_{j=1}^m \left(f(x_i, y_j) + \frac{a_2 x_i + b_2 y_j + d_2}{c_2} \right)^2 \quad (2-9)$$

Then the height deviation $h(x, y)$ of the pavement surface with respect to this mean surface plane is the distance between each point of pavement and the mean surface, which is determined by

$$h(x, y) = \frac{a_2 x + b_2 y + c_2 f(x, y) + d_2}{\sqrt{a_2^2 + b_2^2 + c_2^2}}, \quad x \in [x_a, x_b], y \in [y_a, y_b] \quad (2-10)$$

And the root mean square height is defined by

$$\sigma_h = \sqrt{\frac{1}{A} \int_{y_a}^{y_b} \int_{x_a}^{x_b} h(x, y)^2 dx dy} \quad (2-11)$$

in which the A is the area of the study pavement surface, and is calculated by

$$A = (y_b - y_a)(x_b - x_a) \quad (2-12)$$

Considering the discontinuity of the point cloud, the RMS height is calculated by

$$\sigma_h = \sqrt{\frac{1}{N} \sum_{i=1}^N h(x_i, y_i)^2} \quad (2-13)$$

in which the N is the number of the points in the point cloud.

Using RMS height to describe macrotexture has two advantages. First, the smaller the size of the material applied to the pavement, the smaller the RMS height will be, which is similar to MPD. The finer the material, the smaller the MPD. Second, for the same pavement material, the RMS height is also reflecting the effect of the aggregate loss, whereas the MPD would only show minimal change as the aggregate loss develops.

2.1.3 Aggregate loss percentage

Aggregate loss happens in pavement when the bond between the cement and the aggregate begins to weaken. As the bond continues to decrease, the fine aggregate strips and then the coarse aggregate strips decrease as well. There is not a well-accepted method for quantifying pavement aggregate loss. To evaluate the aggregate loss, this thesis uses the aggregate loss percentage, denoted as a , which is the ratio of the weight of the remaining material denoted as W and the weight of the material without any loss denoted as W_0 . The aggregate loss percentage is determined via

$$a = \frac{W}{W_0} \quad (2-14)$$

If the density of the pavement material can be treated as a constant ρ , the aggregate loss percentage is represented as

$$a = \frac{V}{V_0} \quad (2-15)$$

Since the weight of the aggregate in the pavement is difficult to measure, the aggregate percentage is difficult to measure directly in practice. In this thesis, two approaches are proposed to evaluate the aggregate percentage.

The first approach is determining the relationship between the aggregate percentage and the macrotexture depth (Li et al. 2012), for example, using RMS height (σ_h). Then, the aggregate loss can be deducted from the measurable macrotexture depth. As we discussed earlier, for the same material, the RMS height and aggregate loss percentage (a) are two related variables. The larger the RMS height, the larger the aggregate loss percentage, and the aggregate loss percentage should lean toward 0 as the RMS height close to 0. Accordingly, two possible relationships may meet the requirements. One is the linear equation, see Equation 2-16, the other one is exponential equation, see Equation 2-17. In this thesis, both two are calculated and evaluated, and it will be shown later that the exponential relationship is a better expression of the relationship than the linear one.

$$a = A_1\sigma_h + B_1 \quad (2-16)$$

or

$$a = A_2\exp(B_2\sigma_h) \quad (2-17)$$

The second method evaluates the aggregate percentage by its physical meaning represented by Equation 2-15. The key is measuring the volume of aggregate in the pavement from the 3D model generated from the images. Due to the aggregate loss, those areas lacking aggregate particles would become flat with respect to its surroundings, which is illustrated in Figure 2.2 and the volume of the remaining aggregate could be calculated from those non-flat areas. The measurement procedure includes the following steps:

- (1) generate the 3D model from multi-view images through SfM and MVS;
- (2) determine the flat areas;
- (3) calculate the volume of the remaining aggregates with respect to different aggregate loss percentages by calculating the volume of the non-flat areas;
- (4) find the relationship between the calculated volume and the aggregate loss percentage.

The relationship between volume (V) and the aggregate loss percentage (a) follows the same pattern as the relationship between macrotexture and aggregate loss percentage. The larger the aggregate loss percentage, the larger the calculated volume, and the calculated volume is supposed to approach 0 when the aggregate loss percentage tends to 0. Therefore, both the linear equation, see Equation 2-18, and exponential equation, see Equation 2-19, are capable to describe the relationship between the calculated volume and the aggregate loss percentage. The following results will show that the exponential equation performs better than the linear equation. Moreover, it will be shown that the RMS height holds a stronger relation to the aggregate loss percentage, and it is recommended to calculate aggregate loss through RMS height instead of using calculated volume.

$$a = A_3V + B_3 \quad (2-18)$$

or

$$a = A_4 \exp(B_4V) \quad (2-19)$$

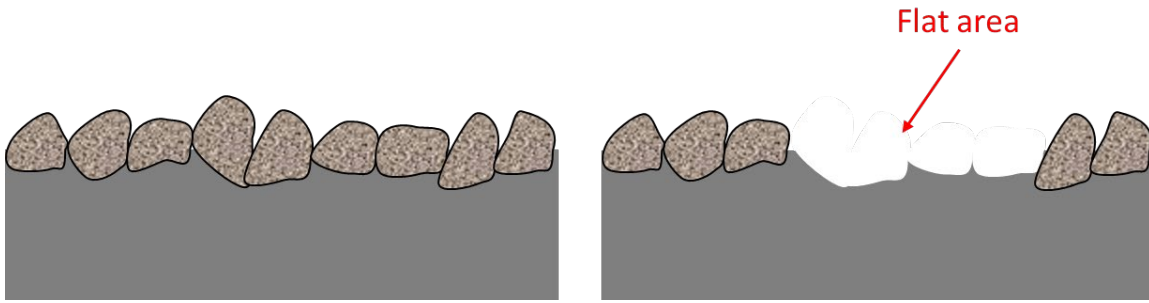


Figure 2.2. Illustration of an intact pavement surface (left) and a pavement surface with serious aggregate loss (right).

2.2 Methodology

This section introduces the techniques for 3D model generation and analysis used in this thesis. First, SfM is introduced. Although the implementation steps of the SfM method vary depending on the software packages used, from image acquisition to georeferenced dense point cloud, the SfM method has the following three major steps.

2.2.1 Keypoint generation

The SfM method aims to identify the common features in consecutive images collected from different angles to estimate the interior and exterior orientation parameters for each camera

position. Therefore, the first step in SfM implementation is to detect, describe, and match the corresponding keypoints between different image-frames. For this purpose, the Scale-Invariant Feature Transform (SIFT) algorithm, which is invariant to image scaling, translation, and rotation and partially invariant to illumination changes and affine or 3D projection, is proposed (Lowe 1999; Lowe 2004). SIFT was the most appealing descriptor when it was proposed and has had a remarkable performance when it was compared to other descriptors. It is still widely used; however, high dimensionality of the descriptor, which prevents faster results, especially for on-line applications, is its drawback at the matching step (Bay et al. 2006). Therefore, newer versions have been proposed that aim to reduce the complexity of the SIFT method while increasing the speed. The Speeded up Robust Features (SURF) algorithm is based on properties similar to SIFT and relies on local gradient histograms; however, it uses integral images to reduce the complexity and to speed up the process (Calonder et al. 2010). Upright-SURF (U-SURF), which is a scale invariant only version of SURF, assumes camera position horizontal, making the SURF algorithm not invariant to image rotation to make the algorithm even faster. Other algorithms proposed to further increase the speed of SURF and SIFT algorithms include the Binary Robust Independent Elementary Features (BRIEF) proposed by Calonder et al. 2010; Oriented FAST and Rotated BRIEF (ORB), which was based on BRIEF (Rublee et al. 2011); (Binary Robust Invariant Scalable Keypoints (BRISK) proposed by Leutenegger et al. 2011); and Brief and Efficient SIFT Image Matching Algorithm (BE-SIFT) proposed by Zhao et al. 2015). The SIFT algorithm deals with the invariance to translation, rotation, and scale, which are four of the six parameters of an affine transform.

As described, all the above algorithms consist of two parts: 1) keypoint detection and 2) keypoint description. For example, the SIFT algorithm includes the SIFT detector and SIFT descriptor. The detector is used to detect the keypoints on the images. Figure 2.3 is an example of all the detected keypoints in one image; and 295,408 keypoints are detected in this photo, which are represented by colored dots. The descriptor is conducted for describing the keypoints and matching these keypoints by calculating the distance between two points on different images. This unique descriptor assures that the keypoints are invariant even after rotation, shift, and scaling. After applying the keypoint detection to all the images, the next step is matching the correspondence between all keypoints on each image. Figure 2.4 illustrates the keypoint matching for two images.

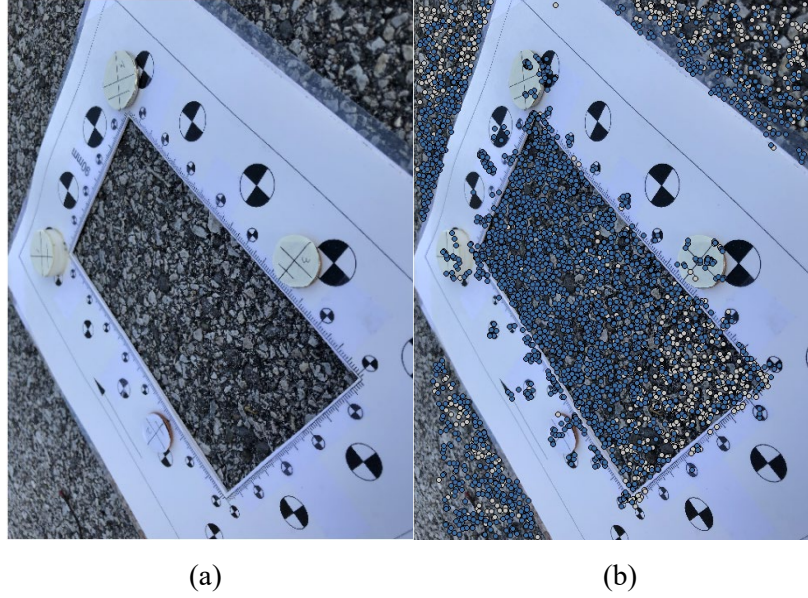


Figure 2.3. Keypoints detection conducted by Agisoft Metashape: (a) original image, and (b) 295,408 keypoints detected for this image.

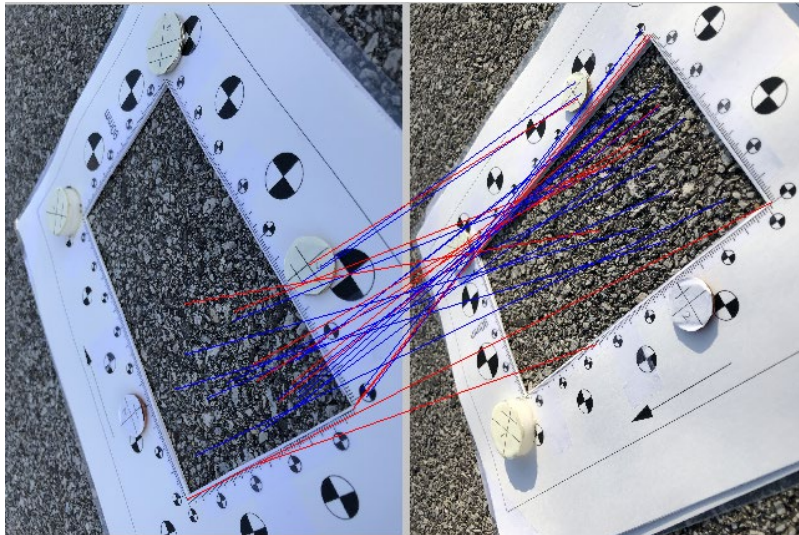


Figure 2.4. Keypoint matching between two images.

2.2.2 Bundle adjustment

In the second step, the interior and exterior orientation parameters for each camera are estimated using the feature correspondences and bundle-adjustment algorithm to estimate the 3D geometry of the scene. At this stage, the SfM method differs from conventional photogrammetry in that SfM does not require GCPs in the scene and separate camera calibration and takes advantage

of the redundancy provided by the large number of images and keypoints to estimate the exterior orientation, interior orientation, and distortion parameters (Smith et al. 2016). The output of this process is an unscaled sparse point cloud having an arbitrary coordinate system as well as the relative position and orientation of each camera to the object, which is shown in Figure 2.5.

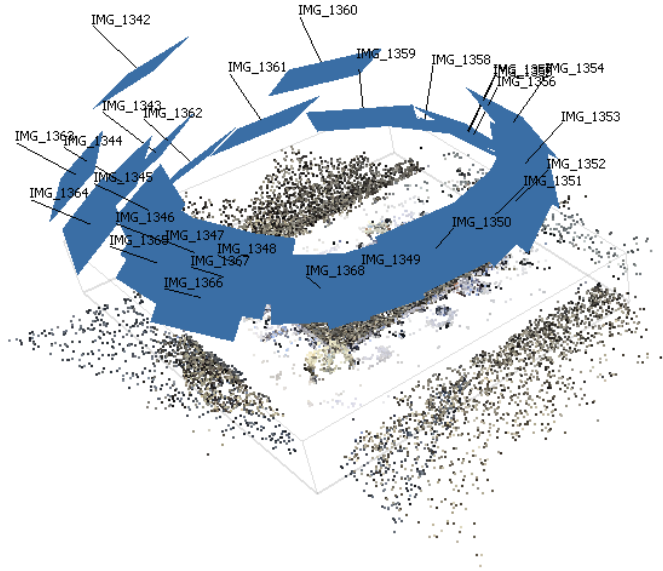


Figure 2.5. Output of bundle adjustment. The dark points are sparse point cloud generated for the object, and the blue rectangles represent the position and orientation of all the images at the time it exposed.

2.2.3 Dense point cloud generation

In the last step, the point density is increased by implementing Multi-View Stereo (MVS) photogrammetry algorithms. Figure 2.6 illustrates the dense point cloud generated from the sparse point cloud. The purpose of the algorithms is to reconstruct the 3D model of an object using overlapped images collected from different viewpoints and known camera positions (Seitz et al. 2006). A wide variety of MVS algorithms were proposed in the literature, which include the following: Photorealistic Scene Reconstruction by Voxel Coloring (Seitz and Dyer 1997, Seitz and Dyer 1999); Patch-based MVS (PMVS) proposed by Furukawa and Ponce 2007, Furukawa and Ponce, 2010a; and Bundled Depth-map Merging for MVS proposed by Li et al. 2010. In fact, the SfM method ends in the second step outlined above where the sparse point cloud is generated. If a dense point cloud is also required in the application, and this is obtained with an MVS algorithm, then the name of this method becomes SfM-MVS.

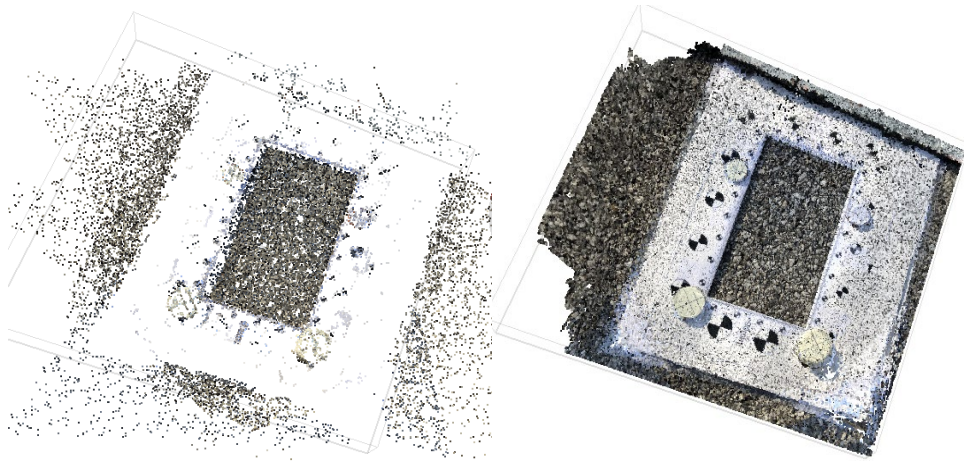


Figure 2.6. Sparse point cloud (left) and the dense point cloud (right). There are 29,132 points in the sparse point cloud, and after densifying the number of points, the dense point cloud can extend to 38,510,294.

The generated point cloud has an arbitrary coordinate system and can be georeferenced by providing at least three additional GCPs. As specified above, these GCPs do not need to be marked in the field. The features that are clearly visible on the image with known 3D coordinates also can be used as GCPs.

2.2.4 Image-based MPD calculation

After the point cloud of the study area is generated, MPD can be calculated following the methods discussed in Section 2.1.1.

Ten profiles are measured by LTS for each spot, and the spacings between adjacent profiles are calculated. This is achieved by reading the LTS output file to get the spacings between adjacent profiles, see Table 2.1. To be consistent with the calculation of LTS, we take 10 profiles along the road direction for each spot and maintain the same spacings between adjacent profiles as LTS. For each profile, the MPD calculation includes following steps (ASTM 2009).

- (1) Filter the profile and preserve the texture wavelengths ranging from 0.5 mm to 50 mm horizontally only;
- (2) Derive the average level by least squares as discussed in Section 2.1.1;
- (3) Divide the profile into two equal segments and calculate the MSDs by finding the maximum height deviation of the segments as Equation 2-5;
- (4) The average of the two MSDs is the MPD for this profile.

For each spot we can get 10 MPDs for 10 profiles, and the MPD for this spot is determined by the average of these 10 MPDs.

Table 2.1. Spacing between adjacent profiles obtained from LTS.

Adjacent profiles	1-2	2-3	3-4	4-5	5-6	6-7	7-8	8-9	9-10
Spacing (mm)	7.9174	8.3255	8.621	8.7999	8.8599	8.8001	8.6213	8.326	7.9181

2.2.5 RMS height calculation

Calculation of the RMS height includes following steps.

- (1) Deduct the mean surface plane of the 3D model of the pavement using least squares method by Equation 2-9;
- (2) Calculate the height deviation $h(x, y)$ with respect to the mean surface plane deducted in step (1) by Equation 2-10;
- (3) Since the discontinuity of the point cloud, the RMS height is calculated via Equation 2-13.

2.2.6 Point cloud segmentation

The original Otsu's method proposed by Otsu in 1979 is applied to image segmentation. It separates objects from the background based on a characteristic that the gray levels of pixels belonging to the object are substantially different from the gray levels of the pixels belonging to the background. Otsu suggested minimizing the weighted sum of within-class variances of the foreground and background pixels to establish an optimum threshold (Otsu 1979). The minimization of the within-class variances is tantamount to the maximization of between-class scatter (Otsu 1979, Sezgin 2004).

Based on the theory of Otsu's method, it can be applied to point cloud segmentation. The height deviation of the point cloud from the multi-view images can be regarded as the gray levels of the pixels, and Otsu's method thus could be implemented to separate the pavement particles from the ground surface. The adapted formulations and evaluation of Otsu's method are discussed below in detail (Otsu 1979).

Given a point cloud with N points in total, suppose we want to separate it into two classes C_0 and C_1 , the optimal threshold is determined by maximizing the between-classes variance σ_B^2 :

$$\sigma_B^2 = \omega_0(\mu_0 - \mu_T)^2 + \omega_1(\mu_1 - \mu_T)^2 \quad (2-20)$$

in which the ω_0 and ω_1 are the probabilities of these two classes, the μ_0 and μ_1 are the means of these two classes, and the μ_T is the total mean of all points.

Assume the variance of all points is denoted as σ_T^2 , an effective metric can be calculated to evaluate the goodness of the threshold:

$$\eta = \frac{\sigma_B^2}{\sigma_T^2} \quad (2-21)$$

It is noticed that η ranges from 0 to 1, and the larger the value of η the larger the between-classes variance, which means the better the performance of the thresholds (Otsu 1979). Moreover, Otsu's method can be extended to multi-classes thresholding (Otsu 1979, Liao 2001, Huang 2009). To classify into k classes, the between-classes are determined by

$$\sigma_B^2 = \sum_{i=1}^k \omega_i(\mu_i - \mu_T)^2 \quad (2-22)$$

The point cloud segmentation in this thesis includes following steps.

- (1) Find the optimal number of classes k using the effective metric in Equation 2-21;
- (2) Segment the point cloud into k classes using the optimal thresholds determined by Otsu's method;
- (3) Reclassify the k classes into 2 classes, one is the flat area of ground surface, the other one is the pavement particle.

Figure 2.7 shows an example of a 3D model of pavement and its segmentation results from Otsu's method. The point cloud is segmented into 5 classes according to the height deviation of each point. To further separate the pavement particle from ground surface, we reclassify these 5 classes into 2 classes. Class 1 is determined to be the flat area of ground surface, and Class 2, 3, 4, and 5 are combined to represent the pavement particle.

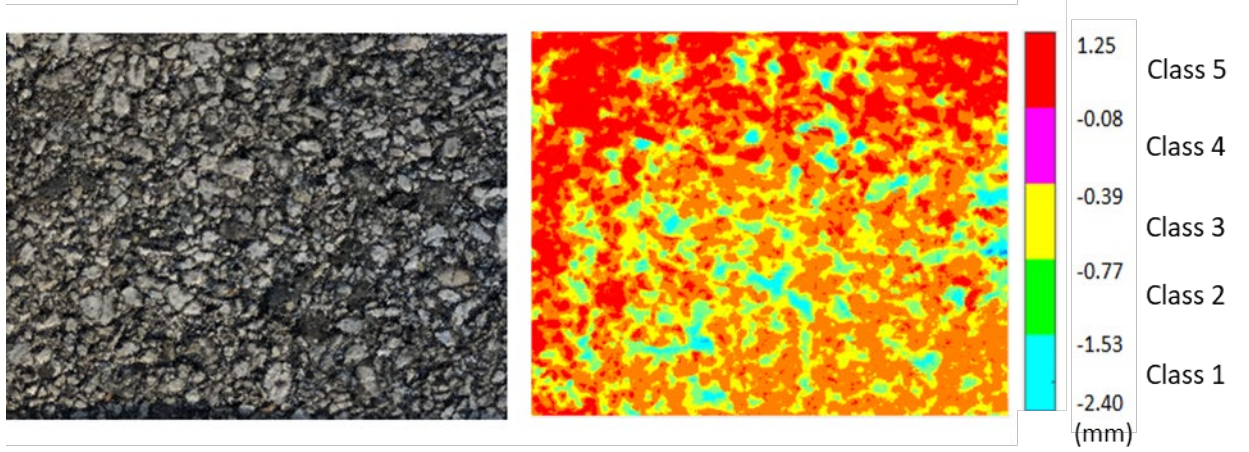


Figure 2.7. Example of a 3D model of pavement (100 mm \times 90 mm) (left) and its height deviation segmentation through Otsu's method (right, mm).

2.2.7 Calculation for the volume of remaining aggregate

We rasterize the point cloud using 0.1 mm \times 0.1 mm grids firstly to calculate the volume of remaining aggregate. The size of the grid is determined by the average ground spacing of the 3D model from images. The ground spacing would be discussed in detail later in Section 3.4. The average ground spacing is 0.074 mm for 38 3D models totally, and the maximum ground spacing is 0.13 mm.

Secondly, assume the average height deviation of the points belonging to the flat area is denoted as h_0 , the relative heights of those points belonging to aggregate particles with respect to flat area, denoted as $H(x, y)$, are obtained by

$$H(x, y) = h(x, y) - h_0 \quad (2-23)$$

According to the number of points within a grid, there are three scenarios for volume calculation, see Figure 2.8. Scenario 1, for a grid that has only one points inside, see Figure 2.8 (a), the volume of this grid (V_1) is calculated by

$$V_1 = 0.01 \times H(x, y) \quad (2-24)$$

Scenarios 2, for a grid contains two points, see Figure 2.8 (b), the volume of this grid is calculated by

$$V_2 = 0.01 \times \frac{1}{2} (H(x_1, y_1) + H(x_2, y_2)) \quad (2-25)$$

Scenario 3, for a grid contains no less than three points, see Figure 2.8 (c), a plane can be determined by these points and the relative heights of the 4 corners of the grid can be calculated, then the volume of this grid (V_3) can be obtained. Finally, the volume of the remaining aggregate is obtained by summing up the volume of grids of all three scenarios, see Equation 2-26.

$$V = \sum(V_1 + V_2 + V_3) \quad (2-26)$$

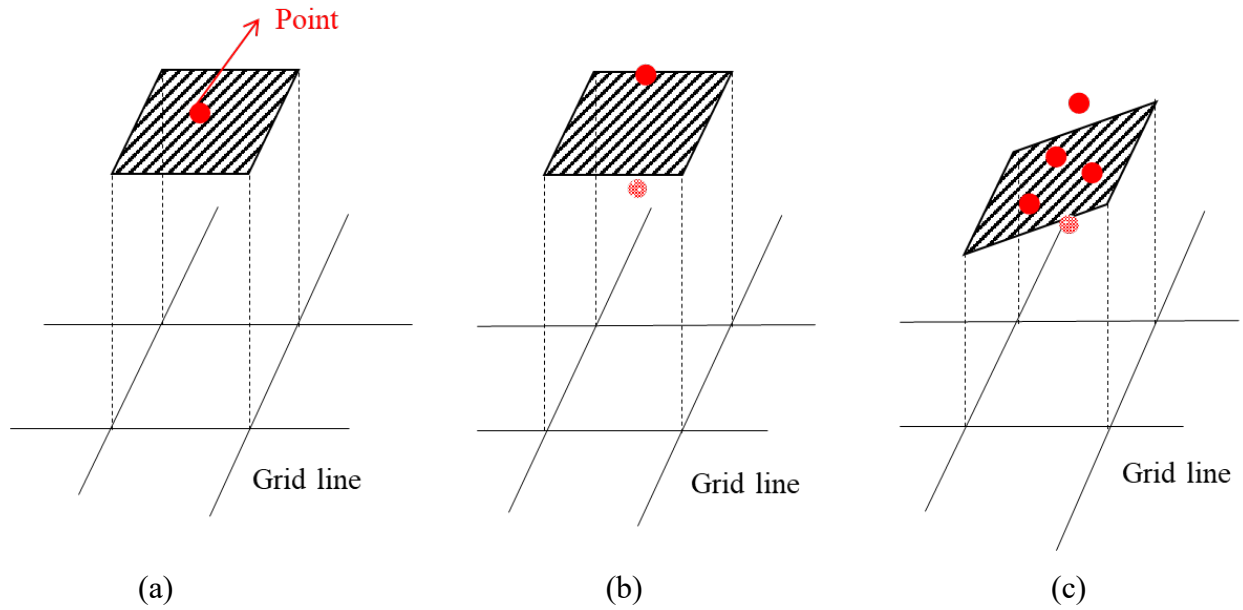


Figure 2.8. Three scenarios for calculating the volume of a grid.

3. EQUIPMENT AND DATA COLLECTION

3.1 Equipment

Both a laser texture scanner and a smartphone were used for data collection. The laser texture scanner used was last calibrated in 2018. The expected MPD measurement range is from 0.5 mm to 2 mm, which is dependent on the material of the pavement and the years of utilization. The classical way to conduct macrotexture measurement is to use a laser texture scanner (LTS). Figure 3.1 shows the Ames LTS Model 9400, which can calculate the pavement's mean profile depth (MPD), texture profile index (TPI), estimated texture depth (ETD), and root mean square (RMS). The characteristics of LTS are listed in Table 3.1. The LTS immediately displays the final results on the LCD display. As for measuring MPD, the LTS can scan ten 100 mm-length-profiles along the road direction, and these ten profiles are unevenly spaced across the road direction. The average point spacing within each profile was 0.014286 mm. The MPD for each profile was calculated and the arithmetic mean of the ten MPDs was considered as the MPD over the area measured. In this study, the LTS was mainly used for measuring the MPD for a pavement surface.



Figure 3.1. LTS model 9400 (left); iPhone 8 plus (right).

Table 3.1. Characteristics of LTS model 9400.

Characteristics	Values	Characteristics	Values
Scan area/mm	107.95×72.01	Triangulation Angle at the center of range	32°
Vertical Resolution/mm	0.015	Dot size at center of range/ μm	50
Maximum Length Resolution/mm	0.015	Dot size at max and min range/ μm	220
Maximum Width Resolution/mm	0.0635	Max laser sampling speed/kHz	1

Table 3.2. Characteristics of iPhone 8 Plus camera.

Characteristics	Values
Wide-angle camera aperture	f/1.8
Telephoto camera aperture	f/2.8
Image dimension	4032 pix \times 3024 pix
pixel size	1.22 μm \times 1.22 μm

The pavement surface images were collected with a commonly used smartphone, the iPhone 8 Plus, which has two 12 MP rear cameras: 1) a wide-angle camera with a f/1.8 aperture and 2) a telephoto camera with a f/2.8 aperture. The wide-angle camera with a f/1.8 aperture is used to collect images in this thesis. The dimension of each image was 4032 pixels \times 3024 pixels. The detailed characteristics of iPhone 8 Plus is shown in Table 3.2. After the images were collected, a 3D point cloud of the pavement surface was reconstructed using Agisoft Metashape.

To provide control and reference for measurement, a control frame was placed in the scene when the images were collected. Two control frames were made. The first control frame A was used as a reference mark for 3D reconstruction when collecting the pavement surface images analyzing MPD on INDOT test site and road sites, as shown in Figure 3.2 (a). The dimension of the central rectangular area is the same size as the LTS, which is 152 mm long and 90 mm wide, and is made of plastically laminated hard paper. There are many marking points on the surface of the template, which are used as references. Moreover, four objects denoted as A1, A2, A3, and A4 with different heights are glued on the template, which are used as the height ruler. The relative heights of these four objects are 8.15 mm, 3.20 mm, 2.90 mm, and 3.36 mm measured by a vernier caliper provides a precision to 0.01 mm, and the distances between each object are measured by the same vernier caliper. Table 3.3 summarizes the measurements of the GCPs on control frame A using the vernier caliper. The dimensions of the rectangular area enclosed by these four objects is the same as the scan area of the LTS, which is 100 mm long and 90 mm wide, to assure that the observation area is consistent for both the LTS and the smartphone.

The second framework B was designed as a reference for analyzing aggregate loss. The dimension of the central rectangular area is 150 mm long and 90 mm wide. The dimension of the entire board is 270 mm long, 180 mm wide, and 5 mm high. Eight objects denoted as B1, B2, B3, B4, B5, B6, B7, and B8 with different heights are glued on the template. The relative heights of these eight objects are 7.5 mm, 10 mm, 7.5 mm, 6.5 mm, 7.5 mm, 10 mm, 7.5 mm and 6.5 mm.

This control frame subsequently printed out via a 3D printer using polylactide material, and the 3D printer used is a Lulzbot Taz 6 printer. See Figure 3.2 (b).

Table 3.3. Summary on the measurements of the GCPs on control frame A.

	Obj.	Measurement 1 (mm)	Measurement 2 (mm)	Measurement 3 (mm)	Average (mm)
Height	A1	8.23	8.13	8.09	8.15
	A2	3.20	3.21	3.20	3.20
	A3	2.92	2.90	2.88	2.90
	A4	3.35	3.40	3.34	3.36
Distance	A1-A2	120.92	120.64	120.72	120.76
	A2-A3	115.07	114.79	114.72	114.86
	A3-A4	119.30	119.48	119.47	119.42
	A4-A1	111.58	111.28	111.25	111.37
	A1-A3	166.32	166.01	165.69	166.01
	A2-A4	164.11	163.97	163.85	163.98

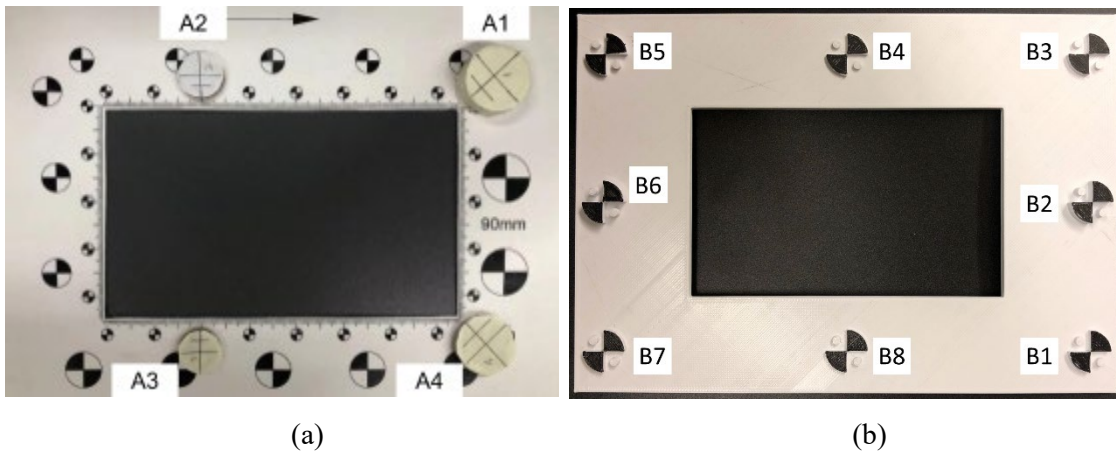


Figure 3.2. Two control frames made for image collection. (a) Control frame A used for collecting images for MPD calculation. (b) Control frame B used for collecting images for aggregate loss analysis.

3.2 Data collection procedure

Since INDOT has been successfully using LTS to measure MPD for several years, the MPD measured by LTS is assumed to be accurate and reliable. Therefore, the MPD by LTS is used to validate the accuracy of the proposed method in this thesis. As shown in Figure 3.3, the data collection procedure for MPD analysis of the proposed method includes following steps.

- (1) Choose a spot randomly and mark the position at the pavement surface.
- (2) Apply control frame A to the spot along the road direction and apply the LTS to that spot, making sure that the laser scans are along the road direction, while scanning the spot and calculating the MPD.
- (3) Remove the LTS, take between 20~32 images for the spot using a smartphone following a circle trace, which is about 400 mm high to the area center and the diameter is about 600 mm.
- (4) Reconstruct the surface based on the images and calculate the MPD from the 3D surface model.
- (5) Move to the next spot and repeat steps (1) to (4) until all spots completed.

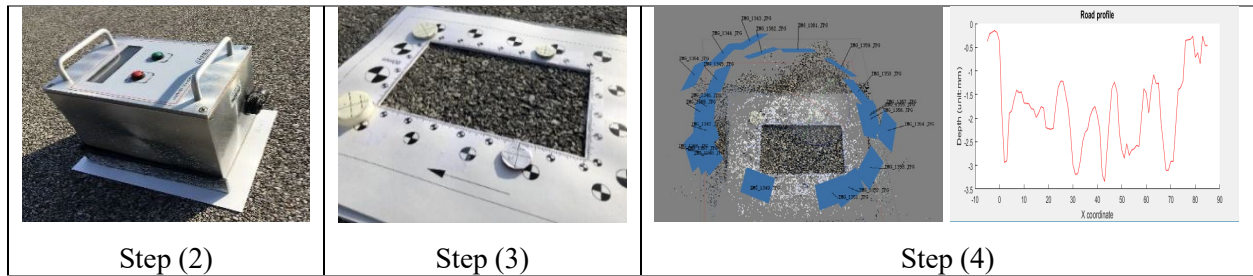


Figure 3.3. Process of data collection on road for MPD measurement.

The data collection procedure for aggregate loss analysis includes the following steps.

- (1) Prepare the samples plates with different aggregate loss percentage.
- (2) Apply control frame B on one sample plate.
- (3) Collect 40 images of the area using a smartphone following a circle trace which is about 400 mm high above the area center and the diameter is about 600 mm.
- (4) Reconstruct the surface based on the images and calculate the MPD from the 3D surface model.
- (5) Move to the next sample plate and repeat steps (2) to (4) steps until completion.

3.3 Sites of data collection

3.3.1 INDOT test site

The test site is located at the INDOT Division of Research and Development, West Lafayette, IN, as shown in Figure 3.4 (a). There are four different types of pavements tested. From Figure 3.4 (b), it can be seen that the righthand lane is Portland cement concrete (PCC) pavement; the center lane is 3-year-old hot-mix asphalt (HMA) pavement; and the lefthand lane is 10-year-old HMA pavement. A 1 m \times 1 m high friction surface treatment (HFST) area is constructed on the 10-year-old HMA pavement. The measurements were performed on the above-mentioned four different pavements on December 3, 2018. For each pavement, there are two testing spots collecting data.



Figure 3.4. Testing site at INDOT.

Table 3.4. Summary of data collected at the INDOT test site spots.

Type of pavement	Date	LTS	Image method	
		Number of spots	Number of spots	Number of images for each spot
10-year-old HMA	12/3/2018	2	2	27
3-year-old HMA	12/3/2018	2	2	22, 29
HFST	12/3/2018	2	2	24, 25

3.3.2 Road sites

State road 32

The HFST on SR 32 was completed on August 13, 2018. Before the HFST, the existing pavement surface was a 9.5 mm HMA mixture. On the day of treatment, the LTS was applied and 11 groups of MPDs were collected for quality control. About eight months after treatment on April 5, 2019 the measurements were collected again at the three testing spots. The detailed information of data collected on SR 32 is shown in Table 3.5, and Figure 3.5 shows a glance of the SR 32. Traffic control was necessary during the measurement process; and due to a time constraint, the LTS and smartphone testing was conducted side by side simultaneously instead of using the exact same locations consecutively.

State road 446

The HFST on SR 446 was finished on October 19, 2018. Before the HFST, the existing pavement surface was single-layer chip seal. On the day of treatment, the LTS was applied and 10 groups of MPDs were collected for quality control. About six months after treatment on April 11, 2019, 10 groups of measurements were collected again. Among the 10 spots, both the LTS and smartphone collected laser data and images at seven spots, and only a smartphone was used to collect images at the other three spots. The detailed information of data collected on SR 446 is shown in Table 3.5, and Figure 3.5 shows a glance of the SR 446. Traffic control was necessary during the measurement process; and due to a time constraint, the LTS and smartphone testing was conducted side by side simultaneously instead of using the exact same location consecutively.

State road 205

The HFST construction at SR 205 was finished on October 23, 2018. Before the HFST, the existing pavement surface was single-layer chip seals. On the day of construction, the LTS was applied and 11 groups of MPDs were collected for quality control. Six months after treatment on April 16, 2019, 12 groups of measurements were collected again. Among these 12 spots, both the LTS and smartphone collected laser data and images. The detailed information of data collected on SR 205 is shown in Table 3.5, and Figure 3.5 shows a glance of the SR 205.



Figure 3.5. Road sites on SR 32 (left), SR 446 (middle) and SR 205 (right).

Table 3.5. Summary of data collected at the test spots on State Roads.

	Day of Construction		After Construction			
	LTS		LTS	Image method		Date 2019
	Number of spots	Date 2018	Number of spots	Number of spots	Number of images for each spot	
SR 32	11	8/13	3	3	20-22	4/5
SR 446	10	10/17	7	10	20-32	4/11
SR 205	11	10/22	12	12	22-29	4/16

3.3.3 Sample plates for aggregate loss analysis

To quantify and analyze the aggregate loss, seven sample plates with different aggregate loss percentages are used. As the aggregate percentage decreased, less material remained on the plate, which simulates the situation when pavement aggregate loss becomes severe. The procedure for preparing the sample plates was as follows.

- (1) Weigh the amount of HFST material needed for a $15\text{ cm} \times 15\text{ cm}$ area for the total weight W_0 .
- (2) Take only part of the total material and apply them on a $15\text{ cm} \times 15\text{ cm}$ plate. The weight of the material actually applied on the plate divided by the total weight W_0 is the aggregate percentage; for example, 12.5% means that 12.5% of the material remains on the sample plate.
- (3) Repeat steps (1) and (2) to make seven sample plates with 12.5%, 25%, 37.5%, 50%, 62.5%, 75% and 100% aggregate, which are shown in Figure 3.6 below

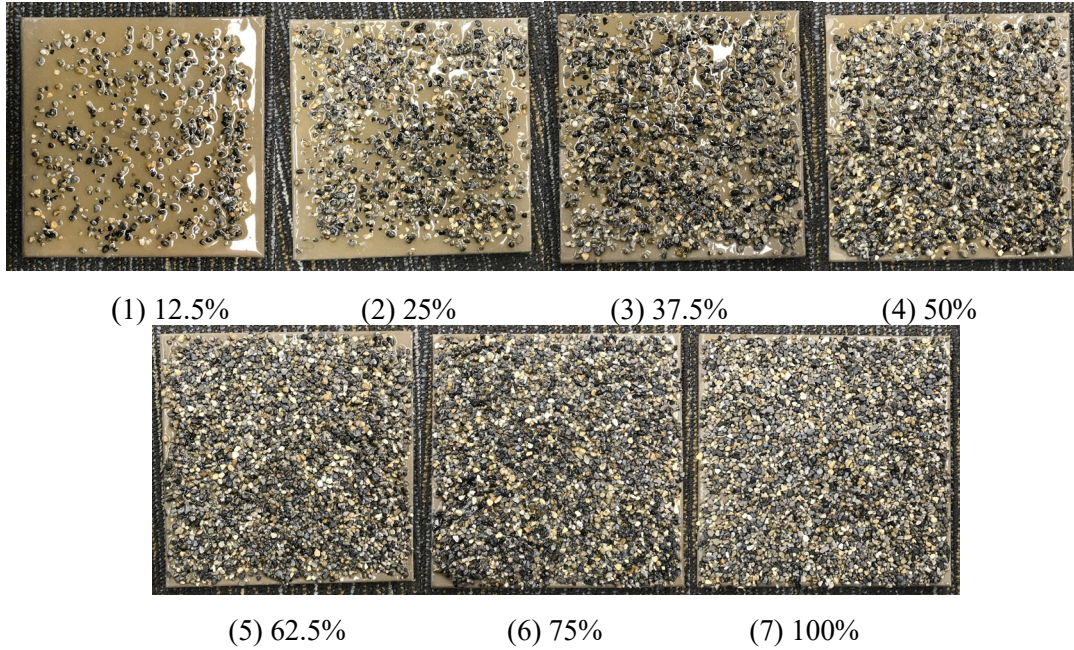


Figure 3.6. Seven sample plates (150 mm×150 mm) for aggregate loss analysis.

3.4 Quality of the 3D models from images

For the MPD calculation, approximately 20 to 32 images were collected at each testing spots and over 700 images were collected in total. Control frame A was used and four ground control points were chosen for georeferencing. The average error of these four GCPs was 1.595 mm along the X direction, 1.077 mm along the Y direction, and 0.133 mm along the Z direction. After georeferencing with the GCPs and densification, 31 3D models with a 517 cm^2 average coverage area were obtained. The average number of points for each point cloud is 10,246,788 and the average ground spacing is 0.071 mm. Once the ground coordinates of the point cloud of the 3D model are computed, these points are reprojected to the pixels on each image using the prior acquired camera position. Thus, the discrepancy between the reprojected pixel and the original pixel is the residual. Based on this concept, the average RMS residual of the tie points is 1.012 mm on the ground and 3.114 pixel on the image, and the average maximum residual of the tie points is 3.167 mm on the ground and 30.890 pixels on the image. Figure 3.7 shows an example of the residual distribution of the tie points. It can be seen that the residuals are in normal distribution in X and Y direction. And the characteristics of this residual distribution also indicates the residuals of the tie points are reasonable, see Table 3.8.

Figure 3.8, Figure 3.9, Figure 3.10, and Figure 3.11 briefly present the 31 3D model generated. It can be seen that the center of the model maintains high quality and the surrounding margin of the model is the part where distortion occurred. This distortion mainly originates from the lens distortion of the original images, which can be seen at the margin of photos. The lens distortion can be largely reduced through lens calibration. In this research, the study area locates at the center of the 3D model, so the lens distortion has minimal impact on calculation. Another noticeable characteristic is the blank area without any points that exists on the white frame. This blank area occurred because no obvious feature points can be detected by SIFT or SURF at the first step of SfM, and the sparse point cloud produces an entire blank area in the dense point cloud.

For aggregate loss analysis, seven sample plates were produced with different aggregate loss percentages, and 40 images were collected from each sample plate for a total of 280 images. Control frame B was used and eight GCPs were chosen for georeferencing. The average error of these eight GCPs was 0.145 mm along the X direction, 0.114 mm along the Y direction, and 0.343 mm along the Z direction. The error of in the GCPs for control frame B in the X, Y direction was significantly less compared to control frame A. The reason for the difference was that the locations of the GCPs on each image for control frame A were selected manually, which enlarged the possibility of error. For control frame B made via a 3D printer, on the other hand, the locations of the GCPs on each image were identified automatically with higher accuracy. The GCP errors for control frame B in the Z direction were slightly larger than control frame A because the z coordinates for control frame A were measured by vernier calipers, and those Z coordinates were used for control frame B as the designed value of the framework. Thus, that error was introduced during the 3D printing.

After georeferencing and densification, seven 3D models with a 435 cm^2 average area were obtained. The average number of points for each point cloud is 7,328,176, and the average ground spacing is 0.077 mm. The average RMS residual of the point cloud is 0.687 mm on the ground and 1.631 pixels on the image; and the average maximum residual of the point cloud is 2.094 mm on the ground and 25.794 pixels on the image. The residual significantly decreased compared to that of the models georeferenced with control frame A. The accuracy of the 3D model is improved by improving the accuracy of the GCPs using control frame B. Figure 3.12 briefly presents these 3D models.

Table 3.6. Average RMS residuals of GCPs used by two control frames.

Control frame	Number of GCPs	Average X residual (mm)	Average Y residual (mm)	Average Z residual (mm)
A	4	1.595	1.077	0.133
B	8	0.145	0.114	0.343

Table 3.7. Summary of the residuals of 3D models.

Control frame	Number of 3D models	Average RMS residual		Average maximum residual	
		mm	pixels	mm	pixels
A	31	1.012	3.114	3.167	30.890
B	7	0.687	1.631	2.094	25.794

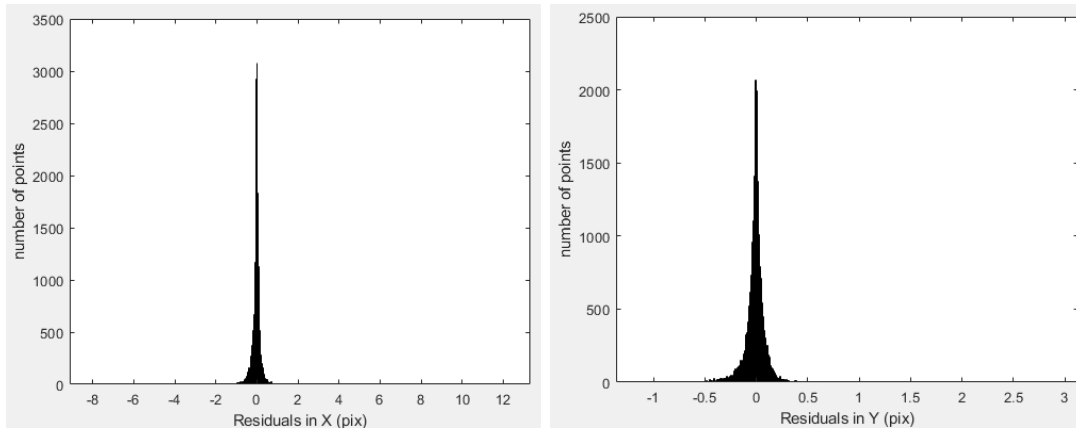


Figure 3.7. Residual distribution of tie points of spot 1 at INDOT test site in X direction (left) and Y direction (right).

Table 3.8. Characteristics of the residual distribution in Figure 3.7.

	Mean μ	STD σ	Points' residual within $\mu \pm \sigma$	Points' residual within $\mu \pm 2\sigma$
Residual in X direction	-0.0273	0.3430	82.56%	95.01%
Residual in Y direction	-0.0117	0.1814	8.50%	95.61%

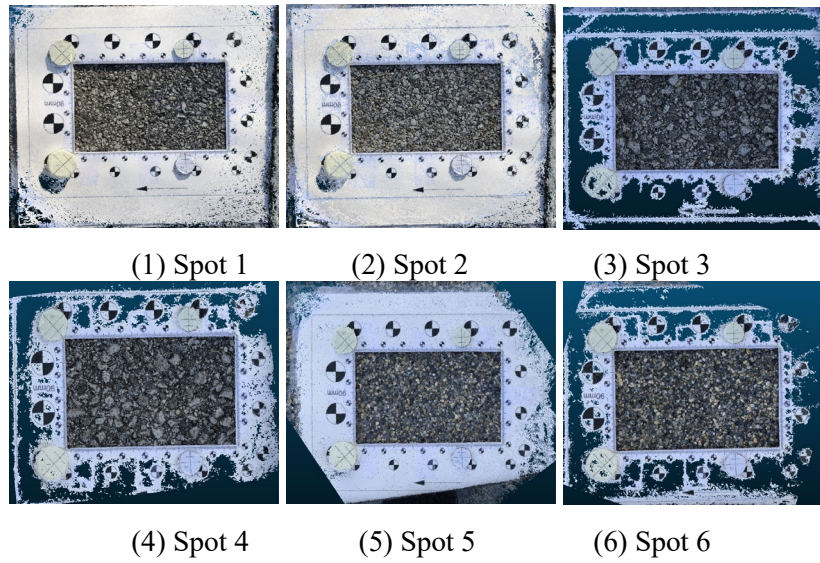


Figure 3.8. Six 3D models for MPD measurement at INDOT test site.

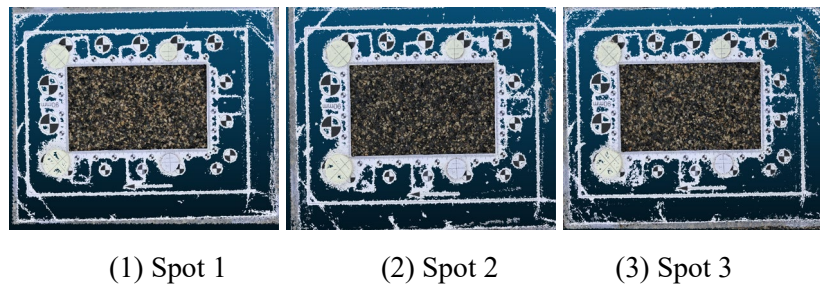


Figure 3.9. Three 3D models for MPD measurement at SR 32.

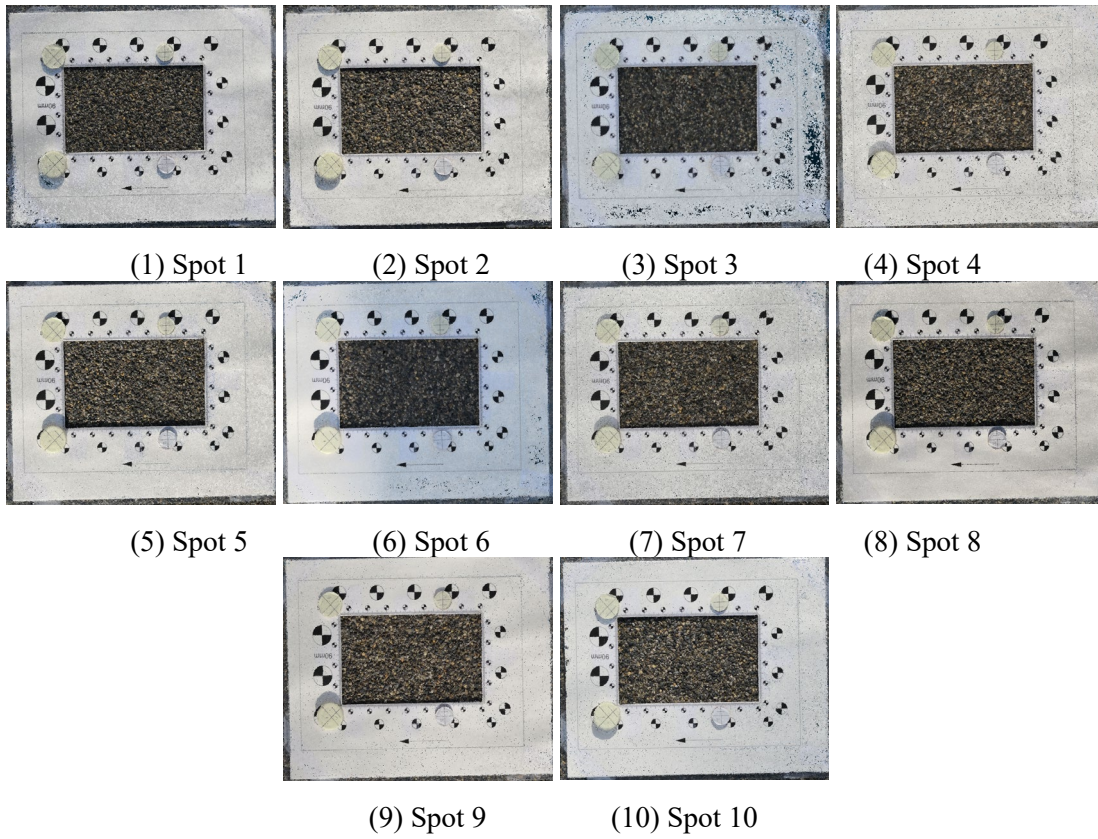


Figure 3.10. Ten 3D models for MPD measurement at SR 446.

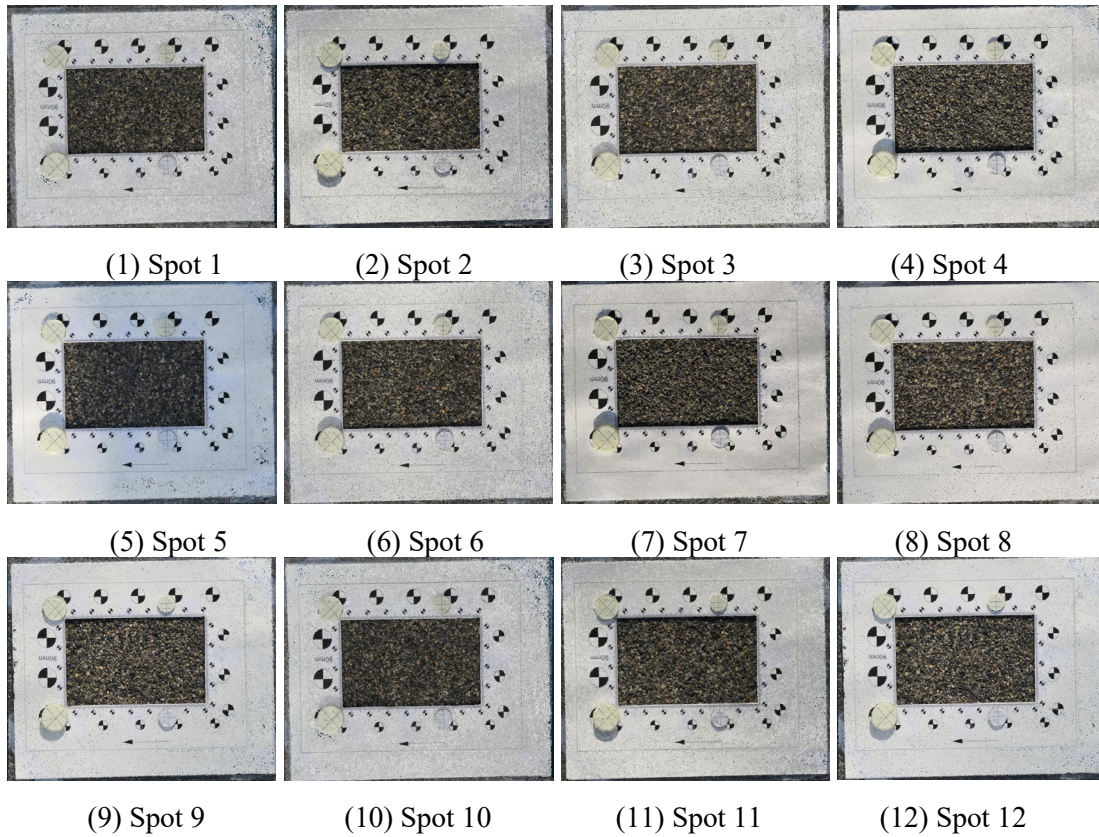


Figure 3.11. Twelve 3D models for MPD measurement at SR 205.

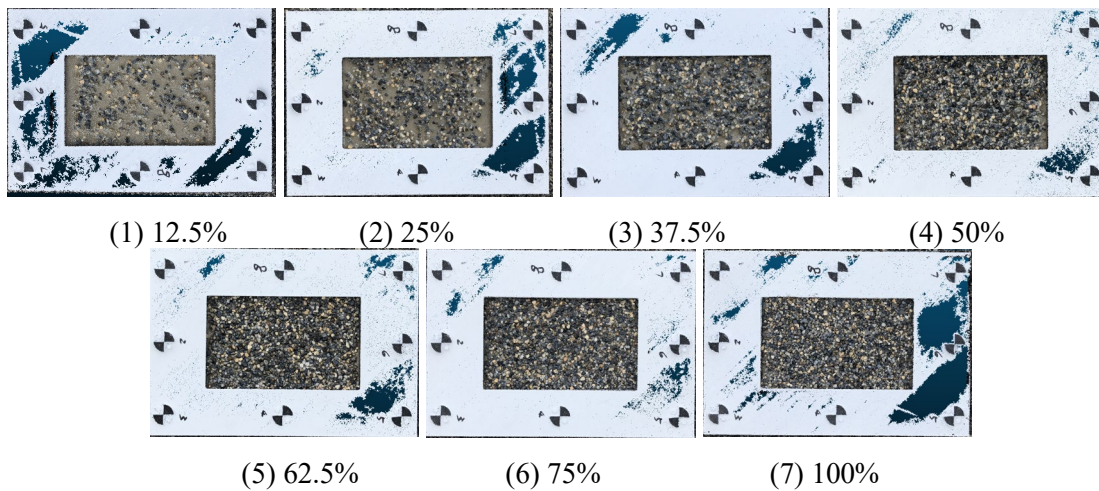


Figure 3.12. Seven 3D models of sample plates for aggregate loss analysis.

4. RESULTS AND EVALUATION

A comparison between the MPD results of the proposed image-based method and LTS is presented in this chapter utilizing the four testing spots in Chapter 3. The results of the aggregate loss evaluation are presented as well.

4.1 MPD results and evaluation

4.1.1 MPD results for test site at INDOT

The first data collection location was the test site located at INDOT, where six pairs of LTS and image data were collected from six different spots at the test site. The MPD results are listed in Table 4.1. Among these six pairs of data, the first two were collected from 3-year-old HMA pavement, the second two pairs were collected from 10-year-old HMA pavement, and the last two pairs were collected from the HFST pavement. The MPD results listed in Table 4.1 are incremental. The MPD of spots 1 and 2 represent the macrotexture of 3-year-old HMA pavement whose average MPD was 0.624 mm. The MPD of spots 3 and 4 represent the macrotexture of 10-year-old HMA pavement whose average MPD was 1.299 mm, which was larger than the 3-year-old HMA pavement's MPD. After 10 years the asphalt had been stripped and the gravel layer was exposed which accounted for its larger MPD than the 3-year old HMA pavement. Finally, the MPD of spots 5 and 6 represent the macrotexture of the HFST pavement, which was larger than that the MPD of both HMA pavements. Accordingly, as the times goes on, the MPD of pavement would decrease first then increase, and the MPD of HFST is improved by 200% compared to the 3-year-old pavement and by 50% with respect to the 10-year-old pavement. Applying HFST on the existing old road is an effective way to increase the pavement friction.

As shown in Table 4.1, the MPD measured by LTS ranged from 0.515 mm to 2.073 mm, and the MPD based on images ranged from 0.559 mm to 2.030 mm. The average MPDs for 3-year-old HMA pavement, 10-year-old HMA pavement, and HFST pavement at the six INDOT testing spots measured by LTS were 0.624 mm, 1.299 mm, and 1.911 mm and the average MPDs based on images were 0.599 mm, 1.316 mm and 1.947 mm, respectively. The difference between the average MPDs for the two methods was less than 6%.

Three spots had differences larger than 10%, and detailed investigations for these three spots therefore were conducted. As mentioned in Section 3.1, the LTS would scan ten profiles during each measurement and take the average of these ten profiles as the MPD for this spot, and the proposed method does the same MPD measurement procedure.

Figure 4.1 shows the calculated MPDs of ten profiles from both LTS and the proposed method for spots 2, 5, and 6 using 3D models. Among these ten profiles, for spot 2, the fifth and eighth profiles show larger discrepancy than the others. The fourth and fifth profiles were blunders for spot 5, and the eighth profile was a blunder for spot 6. It was clearly shown that there were blunders for both the LTS data and the image data, but the average MPDs from both methods were relatively consistent.

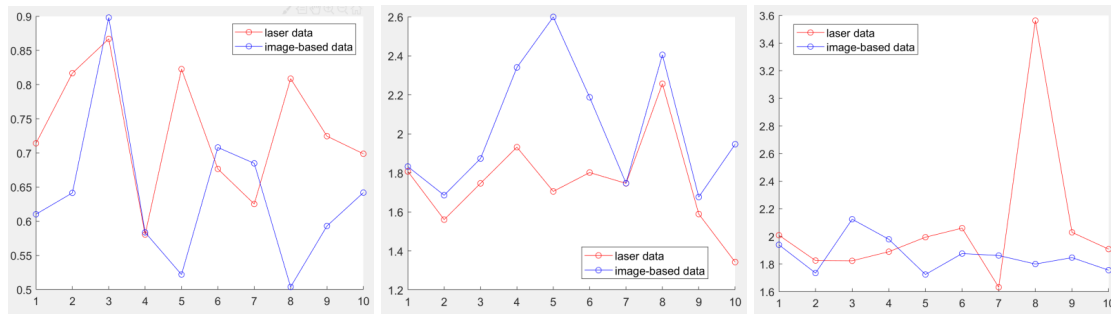


Figure 4.1. Comparison between MPDs of 10 profiles for spot 2 (left), spot 5 (middle) and spot 6 (right) at INDOT.

Table 4.1. MPD from LTS and images for the INDOT test site.

Type of pavement		3-year-old HMA pavement			10-year-old HMA pavement			HFST pavement		
Spot ID		1	2	Avg.	3	4	Avg.	5	6	Avg.
Image method	# of images	27	27		22	29		25	24	
	MPD (mm)	0.559	0.639	0.599	1.244	1.388	1.316	2.030	1.864	1.947
LTS method	MPD (mm)	0.515	0.733	0.624	1.275	1.323	1.299	1.749	2.073	1.911
Difference of MPD (%)		8.6	-12.9	-2.15	-2.4	4.9	1.25	16.0	-10.1	2.95

4.1.2 MPD results for road sites

The MPDs at the three road sites were collected by LTS on the date of the HFST construction, the date for which are shown Table 4.2. According to ASTM E1845, the average MPD measured construction date reflects the macrotexture of the HFST pavement right after construction, which was 2.075 mm, 1.590 mm, and 1.860 mm respectively for SR 32, SR 446, and SR 205. Several months later, these three state road sites were revisited and LTS and images were both collected. Table 4.2 summarized the average MPD measured by LTS and images for each revisited road sites.

Table 4.2. Summary of the MPD of three road sites by LTS and images.

	On Construction		After Construction				
	LTS		Month after	LTS		Image	
	# of spots	Avg. MPD (mm)		# of spots	Avg. MPD (mm)	# of spots	Avg. MPD (mm)
SR 32	11	2.075	7.7	3	1.315	3	1.393
SR 446	10	1.590	5.8	7	1.259	10	1.302
SR 205	11	1.860	5.8	12	1.243	12	1.235

State Road 32

The first road revisited was SR 32 after eight months. Three pairs of LTS and image data were collected from three different spots on SR 32. The results of calculated MPD from both LTS and images are listed in Table 4.3.

State Road 446

SR 446 was the second road revisited after six months, where seven groups of LTS data and ten groups of image data were collected from seven and ten correspondent spots on SR 446. The results of the calculated MPD from both the LTS and the images are listed in Table 4.4.

State Road 205

SR 205 was revisited after six months, where 12 pairs of LTS and image data were collected from 12 different test spots. The results of the calculated MPD from both the LTS and the images are listed in Table 4.5.

Based on the LTS acquisition data on these three state roads, the average MPD of the HFST pavement is 1.272 mm after six to eight months. This is a 30.8% reduction of the MPD after six to eight months of construction compared to the average MPD measured by LTS on the construction

date. According to Tables 4.3, 4.4, and 4.5, there are several large variations of the differences of MPD between two methods among the 22 spots in total. In addition to the blunders, the average MPDs from the proposed image-based method were consistent with the average MPDs from LTS.

Table 4.3. MPD from LTS and image-based methods for SR 32 about 8 months after the construction.

Roads	Spot ID	Image		LTS MPD (mm)	Diff. (%)
		Number of Images	MPD (mm)		
SR 32	1	22	1.401	1.504	-6.8
	2	20	1.562	1.391	12.3
	3	22	1.215	1.05	15.7
Average			1.393	1.315	5.9

Table 4.4. MPD from LTS and image-based methods for SR 446 about 5 months after construction.

Roads	Spot ID	Image		LTS MPD (mm)	Diff. (%)
		Number of Images	MPD (mm)		
SR 446	1	20	1.075	\	\
	2	20	1.143	\	\
	3	29	1.612	\	\
	4	29	1.072	1.178	-9.0
	5	26	1.579	1.353	16.7
	6	26	1.520	1.318	15.3
	7	30	0.913	1.092	-16.4
	8	25	1.524	1.408	8.2
	9	29	1.339	1.201	11.5
	10	32	1.240	1.266	-2.1
Average			1.302	1.259	3.4

Table 4.5. MPD from the LTS and image-based methods for SR 205 about 5 months after construction.

Roads	Spot ID	Image		LTS MPD (mm)	Diff. (%)
		Number of Images	MPD (mm)		
SR 205	1	29	0.944	1.020	-7.4
	2	29	1.025	1.102	-7.0
	3	25	1.003	1.107	-9.4
	4	25	1.167	1.162	0.5
	5	23	1.164	1.195	-2.6
	6	26	1.456	1.222	19.2
	7	25	1.132	1.258	-10.0
	8	26	1.149	1.263	-9.0
	9	26	1.489	1.286	15.8
	10	26	1.201	1.341	-10.5
	11	22	1.693	1.442	17.4
	12	25	1.391	1.516	-8.3
Average			1.235	1.243	-0.9

4.1.3 MPD for any direction

Since the 3D model of pavement already has been reconstructed from images, the MPD for any direction could be calculated for consideration. The profiles of 18 directions were calculated for the MPD. Direction θ ranged from 0° to 180° and was evenly spaced. The direction along the road was set at 0° , and the direction perpendicular to the road was 90° . Figure 4.2 shows the results of the calculated MPD for any direction for the six testing spots at INDOT. Figure 4.2 shows that a direction 10° to the direction along the road has the largest MPD, and the direction perpendicular to the road has the smallest MPD. The results show that the friction across road direction would be largely reduced after a period of traffic and may cause severe safety concern especially at the curves of roads.

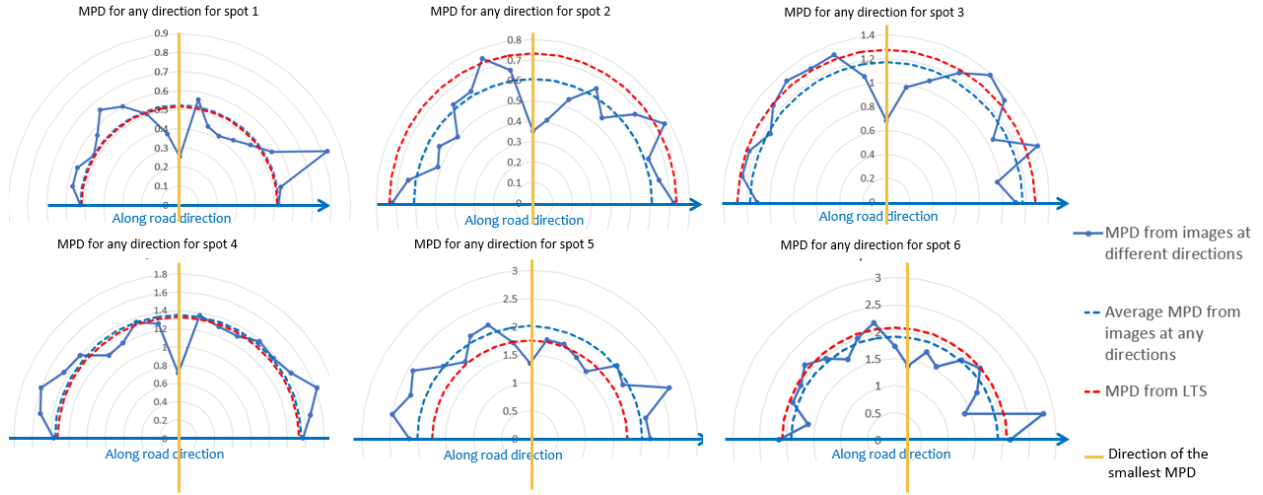


Figure 4.2. MPD for any direction for six testing spots at INDOT.

4.1.4 Summary

The comparison between the MPD results from the LTS and image data was illustrated in the two sections above. 790 images were collected and LTS was conducted at 31 spots. The MPDs from the LTS ranged from 0.515 mm to 2.073 mm, and the MPDs based on images ranged from 0.559 mm to 2.030 mm. The MPD difference at 22 spots of the 31 spots was less than 12% between the two methods, and the maximum MPD difference between the two methods is less than 20%. When the average MPD of each road site was considered, the maximum difference was less than 6%. These discrepancies indicate that when MPD was regarded as expressing the macrotexture of the pavement surface, the MPD calculated based on multiple images by a smartphone was a dependable and economically feasible alternative method compared to LTS.

4.2 Evaluation of Aggregate Loss

4.2.1 Evaluate aggregate loss via RMS height

We will use image-based method for the aggregate loss evaluation. Although MPD is commonly used to describe macrotexture, it cannot reflect the aggregate loss. After the 3D models were reconstructed for the seven sample plates, the MPDs were calculated according to ASTM E1845-09. The MPDs calculated for the seven sample plates with different aggregate loss percentage indicated the limitation of MPD that there were no large discrepancies between the

MPDs for the different aggregate loss situations as can be seen in Table 4.6. As mentioned previously the MPD locates the maximum height deviation of several profiles instead of considering the macrotexture of the entire pavement surface. In other words, very different pavement surface conditions are possibly to have the same MPD.

Table 4.6. Calculated MPD of sample plates with different aggregate loss percentage.

Aggregate Loss Percentage	12.5%	25%	37.5%	50%	62.5%	75%	100%
MPD (mm)	1.224	1.451	1.278	1.279	1.459	1.576	1.540

Therefore, the RMS height will indicate the advantages of describing the macrotexture comprehensively compared to the MPD since it takes all the height deviations of the pavement surface into consideration. The calculated RMS height for each aggregate loss sample plate is shown in Table 4.7. Li et al. stated in 2012 that surface macrotexture can be related to aggregate loss since the excessive aggregate loss will cause catastrophic decrease in macrotexture depth. Theoretically, the sample plate with the smallest aggregate percentage at 12.5% means only that 12.5% of the material remaining has the smallest macrotexture depth, and the sample plate with the largest aggregate percentage of 100% means that no aggregate loss and should have the largest macrotexture depth. The decreasing aggregate loss percentage from 100% to 12.5% therefore would lead to a continuous decrease in the macrotexture depth. The trend of RMS height with respect to different aggregate percentages is illustrated in Figure 4.3 which indicates the relationship between macrotexture and aggregate loss.

Besides aggregate loss, one other aspect to take into consideration regarding macrotexture depth is the particle size of the pavement surface material. The impacts of aggregate loss and particle size on macrotexture depth are independent. In other words, the RMS height and MPD would be different for different material with the same aggregate loss condition and could be identical for different materials with different aggregate loss conditions as well.

The calculated RMS height with respect to different aggregate percentages is shown in Table 4.7 below. As we expected, the RMS height decreases as the aggregate loss percentage decreases.

To find the relationship between aggregate loss percentage and RMS height, we tried two possible fitting as mentioned earlier. The first one is linear regression, see Figure 4.3 (a), and the

linear relationship is determined by Equation 4-1. It is obvious that the linear relationship does not meet the requirement that the predicted aggregate loss percentage is way far from 0 when the RMS height decreases to 0. The exponential fitting is shown in Figure 4.3 (b), and the relationship is determined by Equation 4-2. The exponential equation performs better than linear equation that the predicted aggregate loss percentage approaches 0 as the RMS height tend toward 0. The aggregate loss percentage is possible to be 0 theoretically, but it will never be 0 exactly in practice due to noise from measurement.

$$a = 258.35\sigma_h - 109.37 \quad (4-1)$$

or

$$a = 2.09\exp(4.96\sigma_h) \quad (4-2)$$

Table 4.7. Calculated RMS height of sample plates with different aggregate loss percentage.

Aggregate Loss Percentage	12.5%	25%	37.5%	50%	62.5%	75%	100%
RMS height (mm)	0.509	0.544	0.556	0.696	0.572	0.726	0.765

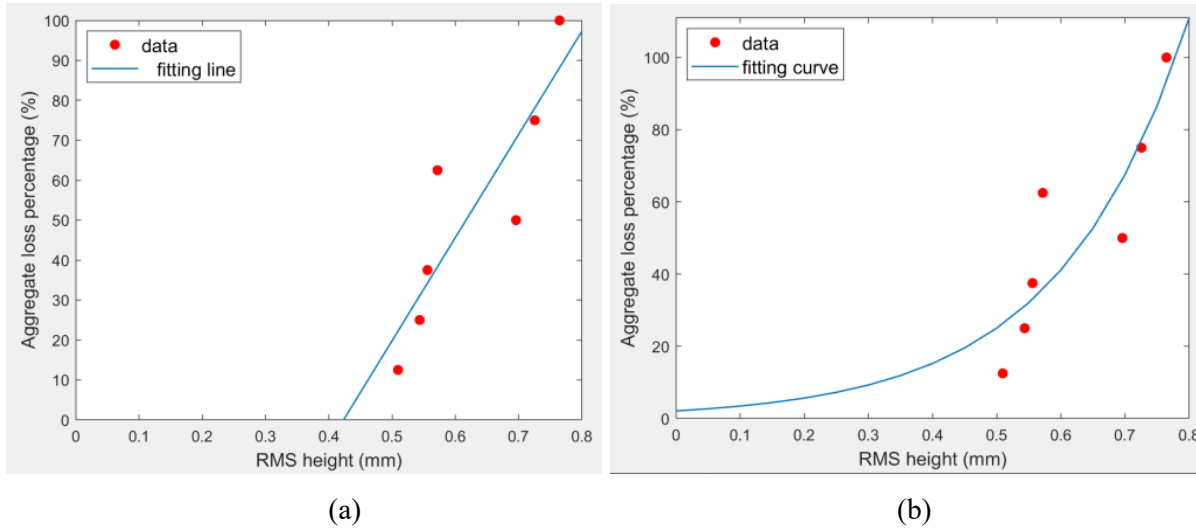


Figure 4.3. Illustration of the relationship between aggregate loss percentage and RMS height using (a) linear regression and (b) exponential fitting.

The exponential fitting is further evaluated quantitatively. Table 4.8 lists the residuals of the exponential fitting. Although the number of residuals is small since small number of sample plates, the average of the residual is 0.5670%, which is close to 0, shows reasonable residuals of the fitting

model. The root mean square error (RMSE) of the exponential fitting is 14.601, and the R-squared is 0.8359 shows that 83.59% of the total variants can be explained by the exponential fitting model.

Table 4.8. Residuals of exponential fitting for aggregate loss percentage on RMS height.

RMS height (mm)	0.509	0.544	0.556	0.696	0.572	0.726	0.765
True aggregate loss percentage	12.5%	25%	37.5%	50%	62.5%	75%	100%
Calculated aggregate loss percentage	26.22%	31.07%	33.02%	66.18%	35.73%	76.66%	93.05%
Residuals (%)	-13.72	-6.07	4.48	-16.18	26.77	-1.66	6.95

4.2.2 Evaluate aggregate loss via volume

Another way to evaluate the aggregate loss besides analyzing the aggregate loss by macrotexture measurement is considering the physical meaning of aggregate loss by its volume. According to Equation 2-12, the ratio of the volume of the remaining aggregate and the volume of the aggregate without any loss among the same area is the aggregate loss percentage. Therefore, we may measure the aggregate loss percentage by finding the relationship between aggregate loss percentage and the volume of the remaining.

Due to excessive aggregate loss, the ground under the first layer of pavement exposed has a flat appearance. To calculate the volume of the remaining aggregate, the first step was to separate the objects from the ground using Otsu's method. One problem that needed to be solved for Otsu's method was the optimal number of classes. We implemented Otsu's method with different numbers of classes for seven sample plates, and the effectiveness was calculated to evaluate the goodness of the thresholding (see Figure 4.4). As the number of classes increased, the effectiveness increased sharply at first and then remained somewhat steady. Suppose the number of classes is denoted as k , the effectiveness of this number of classes is η_k . The best number of classes is the one that satisfies Equation 4-3. The optimal numbers of classes for the seven sample plates are shown in Table 4.9.

$$\frac{\eta_k - \eta_{k-1}}{\eta_{k-1}} < 0.1 \text{ \& } \eta_k > 0.9 \quad (4-3)$$

Figure 4.5 compares the results of Otsu's method and the original model side by side in detail. The point cloud for the 12.5% sample plate is classified into 4 classes, and the others are divided into 5 classes. Further, Class 1 is determined to be the flat area of the ground, and the rest classes are combined to be the remaining aggregate. From Figure 4.5, it can be seen that the area of the ground for a low aggregate percentage was underestimated, such as the 12.5% sample plate, while the area of ground for a high aggregate percentage overestimated, such as the 100% plate. Then, the volumes of the aggregates for the seven sample plates were measured (see Table 4.9).

Table 4.9. Optimal number of classes and volume of aggregate remained on each sample plate.

Aggregate Loss Percentage	12.5%	25%	37.5%	50%	62.5%	75%	100%
Optimal k	4	5	5	5	5	5	5
Volume (cm^3)	27.217	24.817	30.291	34.070	27.288	34.703	39.133

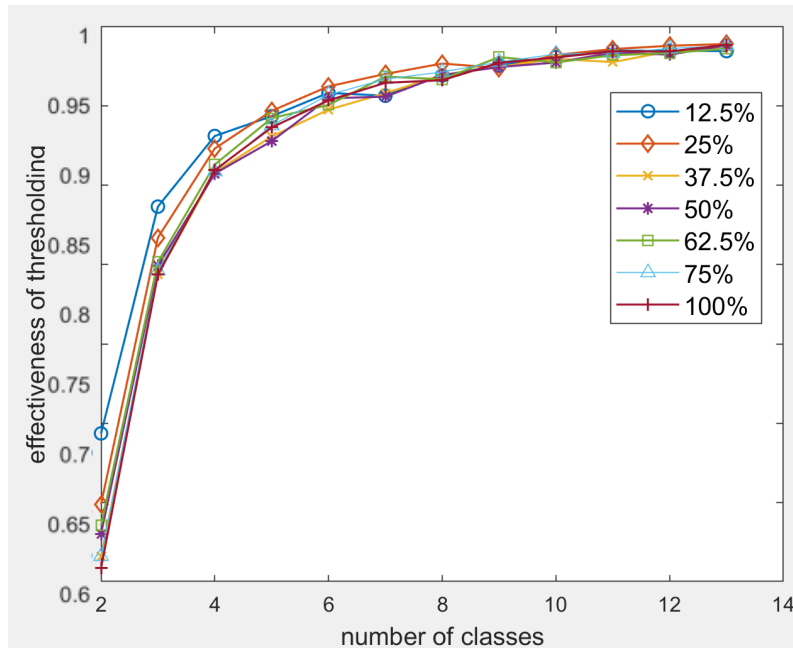


Figure 4.4. Effectiveness of thresholding vs. number of classes for seven sample plates.

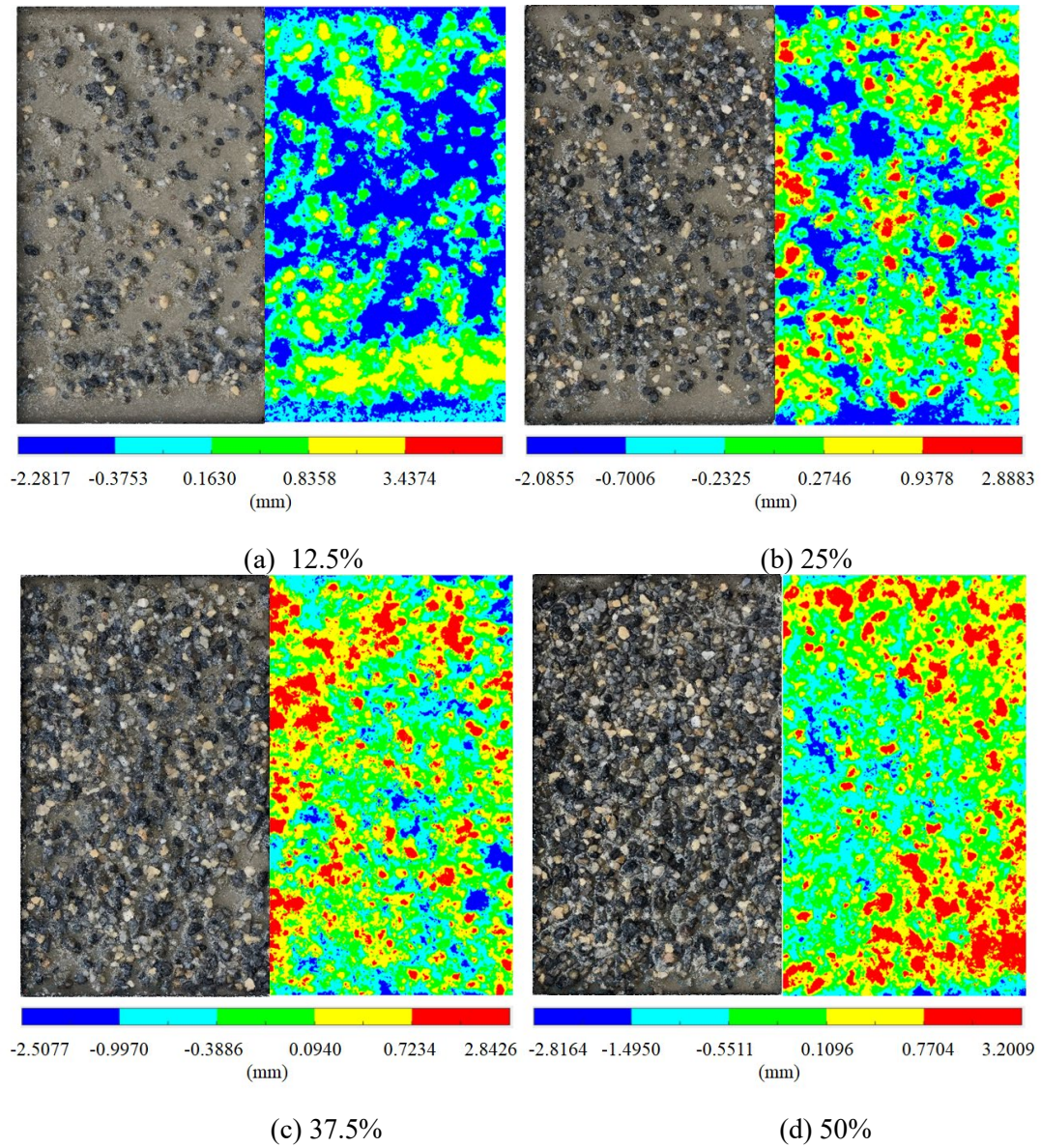
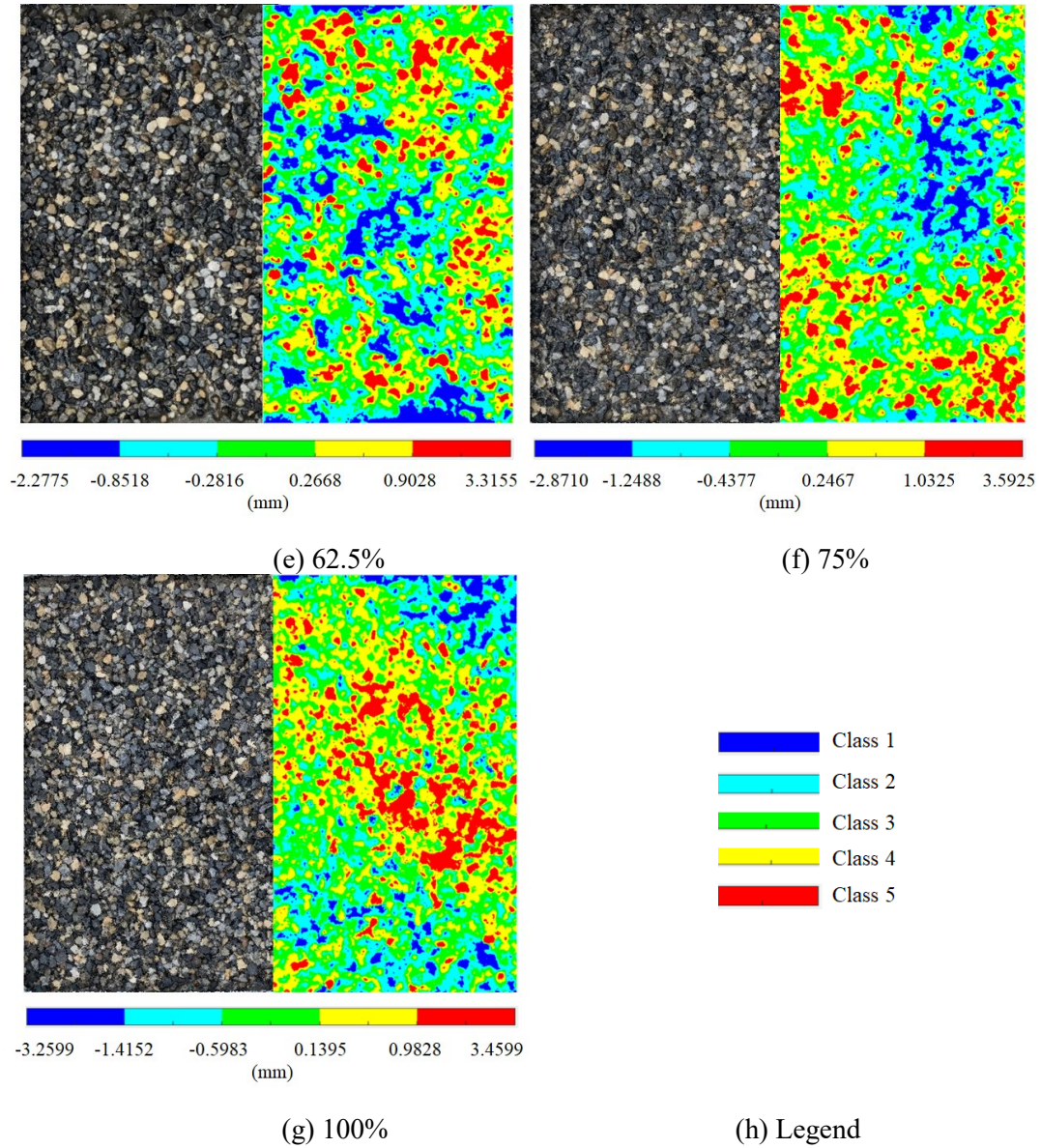


Figure 4.5. Comparison between original 3D model and the thresholding results of Otsu's method for seven sample plates.

Figure 4.5. Continued.



To find the relationship between aggregate loss percentage and volume of the remaining aggregate, we tried two possible fitting too. The first one is linear regression, see Figure 4.6 (a), and the linear relationship is determined by Equation 4-4. Obviously, the linear relationship does not meet the requirement that the predicted aggregate loss percentage is way far from 0 when the volume of the remaining aggregate decreases to 0. The exponential fitting is shown in Figure 4.6 (b), and the relationship is determined by Equation 4-5. The exponential equation performs much better than linear equation that the predicted aggregate loss percentage approaches 0 as the volume

decreases to 0. Theoretically, the aggregate loss percentage should be 0 when the volume is 0, but it will never be 0 exactly practically due to the noise from measurement.

$$a = 4.85 \times 10^{-3}V - 98.98 \quad (4-4)$$

or

$$a = 2.54 \exp(9.37 \times 10^{-2}V) \quad (4-5)$$

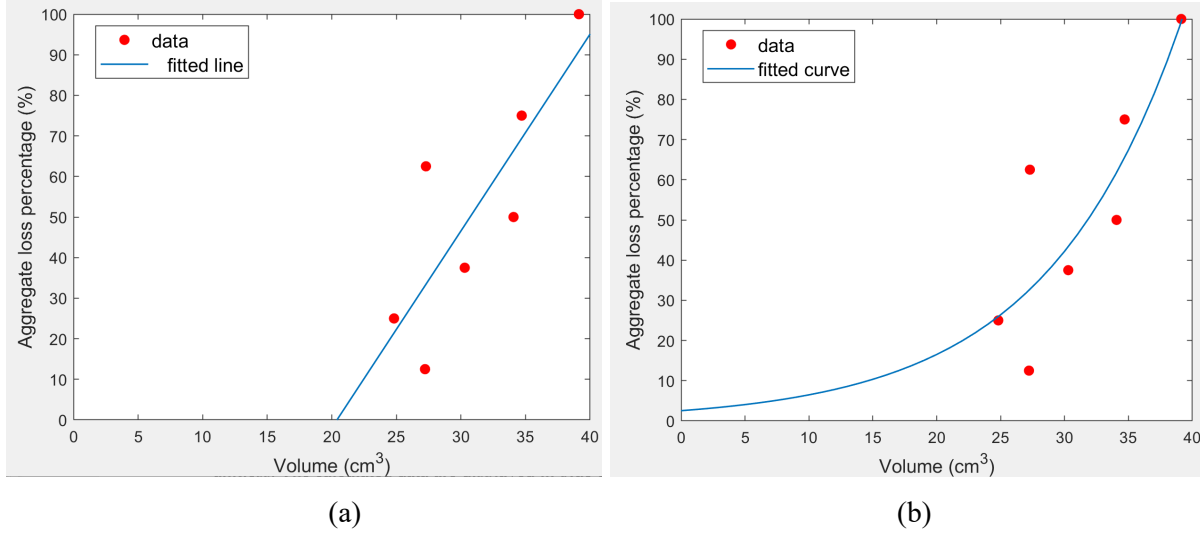


Figure 4.6. Illustration of the relationship between aggregate loss percentage and volume of remaining aggregate using (a) linear regression and (b) exponential fitting.

To evaluate the exponential fitting quantitatively. Table 4.10 lists the residuals of the exponential fitting for the relationship between aggregate loss percentage and volume. The average of the residual is 1.333%, which is close to 0, shows reasonable residuals of the fitting model. The RMSE of the exponential fitting is 16.1086%, and the R-squared is 0.8002 shows that 80.02% of the total variants can be explained by the exponential fitting model.

Table 4.10. Residuals of exponential fitting for aggregate loss percentage on volume.

Volume (cm^3)	27.217	24.817	30.291	34.070	27.288	34.703	39.133
Aggregate Loss Percentage	12.5%	25%	37.5%	50%	62.5%	75%	100%
Calculated aggregate loss percentage	32.5%	25.95%	43.35%	61.78%	32.72%	65.56%	99.3%
Residuals (%)	-20	-0.95	-5.85	-11.78	29.78	9.44	0.70

4.2.3 Summary

Analysis of the measurement of aggregate loss was conducted through two approaches. Seven sample plates were produced with different aggregate percentages. Forty images were collected by iPhone 8 plus for each sample plate for a total of 280 images. Seven fine 3D models were reconstructed from these 280 images. From the calculations, it was determined that there were no large discrepancies between the MPDs for the seven sample plates. In other words, the MPD cannot sufficiently represent the macrotexture of pavements while the RMS height can represent the macrotexture depth and reflect the aggregate loss very well.

Therefore, the first approach evaluated the aggregate loss via determining the relationship between RMS height and aggregate loss percentage. The second approach evaluated the aggregate loss via determining the relationship between the volume of remaining aggregate on the pavement and aggregate loss percentage. Both relationships were fitted by the linear equation and the exponential equation. From the above results, the exponential fitting was found to perform better than the linear fitting. Table 4.11 summarizes the evaluation of two exponential fitting models for both relationships. It can be seen that the exponential fitting model for aggregate loss percentage on RMS height holds a larger R-squared and a smaller RMSE than the other one, meaning the model has a better performance. In summary, aggregate loss is recommended to be measured through RMS height via Equation 4-2.

Table 4.11. Summary of the evaluation of two exponential fitting models.

Exponential fitting model	Average residual (%)	R-squared	RMSE (%)
RMS height vs. Aggregate loss percentage	0.5670	0.8359	14.6008
Volume vs. Aggregate loss percentage	1.333	0.8002	16.1086

5. CONCLUSION

This thesis explored an alternative technology for MPD measurement using multi-view images collected by smartphone. Thirty-one 3D models were reconstructed from over 700 images collected at 31 different spots. The quality of these 3D models was evaluated in Chapter 3. It is known from Chapter 3 that images by smartphone with a well-produced control frame are sufficient for the reconstruction of a high-resolution 3D model. Based on tens of high-resolution 3D models of the pavement surface created by Structure from Motion (SfM) technique, we show that the image-based macrotexture measurement is convenient, cost effective and comparable to the traditional LTS methods in Chapter 4.1. We expect this newly development be further enhanced and adopted widely.

In Chapter 4.2, the limitation of MPD describing macrotexture depth under aggregate loss was addressed and RMS height was conducted for macrotexture depth representation. The RMS height has advantages on comprehensive representing macrotexture depth and reflecting aggregate loss. As for aggregate loss which used to be difficult to measure in practice, this thesis implemented two approaches to evaluate aggregate percentage. The aggregate loss percentage was discovered to be exponential related to RMS height and volume of remaining aggregate. And the exponential relationships between them were derived, the exponential fitting model of aggregate loss percentage on RMS height performs better than the exponential model of aggregate loss percentage on volume. Thus RMS height is recommended for aggregate loss evaluation.

There are several areas where this research could be improved. First, one of the control frames used to take images is handmade by cardboard which is flexible, and another control frame made via 3D printing is slightly bent due to the cooling during printing. The unevenness and bent of control frame limit the quality of the 3D model. A 3D model with higher resolution and better quality can be gained with a more rigid control frame. Second, the number of sample plates for aggregate loss analysis are too small, there is only one sample plate for each aggregate percentage. More sample plates could make the exponential fitting model more reliable, more noise-resistant and more accurate. Third, the sample plates are made of HFST pavement material only. As mentioned earlier, the RMS height depends on aggregate loss percentage and the pavement material. The exponential model deducted before has poor generality for all pavement. It reveals the exponential relationship between aggregate loss percentage and RMS height, while the

coefficients of the model need to be recalculated for the other pavement material. If the sample plates made of variance of material are provided, a more general and more convincing model may be derived.

REFERENCES

- Abulizi, N., Kawamura, A., Tomiyama, K., & Fujita, S. (2016). Measuring and evaluating of road roughness conditions with a compact road profiler and ArcGIS. *Journal of Traffic and Transportation Engineering (English Edition)*, 3(5), 398–411. doi: 10.1016/j.jtte.2016.09.004
- Adams, J., Castorena, C., Im, J. H., Ilias, M., & Kim, Y. R. (2017). Addressing Raveling Resistance in Chip Seal Specifications. *Transportation Research Record: Journal of the Transportation Research Board*, 2612(1), 39–46. doi: 10.3141/2612-05
- Aktaş, B., Gransberg, D. D., Riemer, C., & Pittenger, D. (2011). Comparative Analysis of Macrotexture Measurement Tests for Pavement Preservation Treatments. *Transportation Research Record: Journal of the Transportation Research Board*, 2209(1), 34–40. doi: 10.3141/2209-05
- ASTM E1845-09, Standard Practice for Calculating Pavement Macrotexture Mean Profile Depth, *ASTM International, West Conshohocken, PA, 2015*, www.astm.org
- Babu, G. S., Kandhal, P. S., Kottayi, N. M., Mallick, R. B., & Veeraragavan, A. (2019). Pavement Drainage Structures. *Pavement Drainage*, 43–116. doi: 10.1201/9781351135948-4
- Baqersad, M., Haghigat, A. E., Rowshanzamir, M., & Bak, H. M. (2016). Comparison of Coupled and Uncoupled Consolidation Equations Using Finite Element Method in Plane-Strain Condition. *Civil Engineering Journal*, 2(8), 375–388. doi: 10.28991/cej-2016-00000042
- Bitelli, G., Simone, A., Girardi, F., & Lantieri, C. (2012). Laser Scanning on Road Pavements: A New Approach for Characterizing Surface Texture. *Sensors*, 12(7), 9110–9128. doi: 10.3390/s120709110
- Byrum, C. R., Raymond, C., Swanlund, M., & Kazmierowski, T. (2010). Experimental Short-Wavelength Surface Textures in Portland Cement Concrete Pavements. *Transportation Research Record: Journal of the Transportation Research Board*, 2155(1), 170–178. doi: 10.3141/2155-18
- Calonder, M., Lepetit, V., Strecha, C., & Fua, P. (2010). BRIEF: Binary Robust Independent Elementary Features. *Computer Vision – ECCV 2010 Lecture Notes in Computer Science*, 778–792. doi: 10.1007/978-3-642-15561-1_56
- Cigada, A., Mancosu, F., Manzoni, S., & Zappa, E. (2010). Laser-triangulation device for in-line measurement of road texture at medium and high speed. *Mechanical Systems and Signal Processing*, 24(7), 2225–2234. doi: 10.1016/j.ymssp.2010.05.002
- Das, A., Rosauer, V., & Bald, J. S. (2015). Study of road surface characteristics in frequency domain using micro-optical 3-D camera. *KSCE Journal of Civil Engineering*, 19(5), 1282–1291. doi: 10.1007/s12205-013-0529-3

- Dong, N., Prozzi, J., & Ni, F. (2019). Reconstruction of 3D Pavement Texture on Handling Dropouts and Spikes Using Multiple Data Processing Methods. *Sensors*, 19(2), 278. doi: 10.3390/s19020278
- Douangphachanh, V., & Oneyama, H. (2013). Estimation of road roughness condition from smartphones under realistic settings. *2013 13th International Conference on ITS Telecommunications (ITST)*, 10, 1551–1564. doi: 10.1109/itst.2013.6685585
- Dunford, A. (2013). Friction and the Texture of Aggregate Particles Used in the Road Surface Course, Ph.D. Thesis, University of Nottingham
- Ejsmont, J. A., Ronowski, G., Świczko-Żurek, B., & Sommer, S. (2016). Road texture influence on tyre rolling resistance. *Road Materials and Pavement Design*, 18(1), 181–198. doi: 10.1080/14680629.2016.1160835
- Ergun, M., Iyınam, S., & Iyınam, A. F. (2005). Prediction of Road Surface Friction Coefficient Using Only Macro- and Microtexture Measurements. *Journal of Transportation Engineering*, 131(4), 311–319. doi: 10.1061/(asce)0733-947x(2005)131:4(311)
- Fisco, N., & Sezen, H. (2014). Comparison of Surface Macrotexture Measurement Methods. *Journal of Civil Engineering and Management*, 19(Supplement_1), 153–160. doi: 10.3846/13923730.2013.802732
- Flintsch, G., León, E., McGhee, K. & Al-Qadi, I. (2003). Pavement Surface Macrotexture Measurement and Applications. *Transportation Research Record*. 1860. 168-177. doi: 10.3141/1860-19
- Furukawa, Y., & Ponce, J. (2007). Accurate, Dense, and Robust Multi-View Stereopsis. *2007 IEEE Conference on Computer Vision and Pattern Recognition*. doi: 10.1109/cvpr.2007.383246
- Gendy, A. E., Shalaby, A., Saleh, M., & Flintsch, G. W. (2011). Stereo-vision applications to reconstruct the 3D texture of pavement surface. *International Journal of Pavement Engineering*, 12(3), 263–273. doi: 10.1080/10298436.2010.546858
- Gransberg, D. D. (2008). Evaluate TXDOT Chip Seal Binder Performance Using Pavement Management Information System and Field Measurement Data San Antonio District. *Interim Research Report No. 3. University of Oklahoma, Norman, OK*.
- Gransberg, D. D., & James, D. M. B. (2005). Chip seal best practices. In *Chip seal best practices*. Washington, D.C.: Transportation Research Board.
- Henry, J. J. (2000). Evaluation of Pavement Friction Characteristics. *Transportation Research Board*, (291), 0547–5570. Retrieved from <http://worldcat.org/isbn/0309068746>
- Huang, D.-Y., & Wang, C.-H. (2009). Optimal multi-level thresholding using a two-stage Otsu optimization approach. *Pattern Recognition Letters*, 30(3), 275–284. doi: 10.1016/j.patrec.2008.10.003

- Kanafı, M. M., Kuosmanen, A., Pellinen, T. K., & Tuononen, A. J. (2014). Macro- and micro-texture evolution of road pavements and correlation with friction. *International Journal of Pavement Engineering*, 16(2), 168–179. doi: 10.1080/10298436.2014.937715
- Kogbara, R. B., Masad, E. A., Woodward, D., & Millar, P. (2018). Relating surface texture parameters from close range photogrammetry to Grip-Tester pavement friction measurements. *Construction and Building Materials*, 166, 227–240. doi: 10.1016/j.conbuildmat.2018.01.102
- Leutenegger, S., Chli, M., & Siegwart, R. Y. (2011). BRISK: Binary Robust invariant scalable keypoints. *2011 International Conference on Computer Vision*. doi: 10.1109/iccv.2011.6126542
- Li, L., Wang, K. C., & Li, Q. (2016). Geometric texture indicators for safety on AC pavements with 1mm 3D laser texture data. *International Journal of Pavement Research and Technology*, 9(1), 49–62. doi: 10.1016/j.ijprt.2016.01.004
- Li, S., Shields, T., Noureldin, S., & Jiang, Y. (2012). Field Evaluation of Surface Friction Performance of Chip Seals in Indiana. *Transportation Research Record: Journal of the Transportation Research Board*, 2295(1), 11–18. doi: 10.3141/2295-02
- Liao, P., Chen, T., Chung, P.. (2001). A Fast Algorithm for Multilevel Thresholding. *Journal of Information Science and Engineering*. 17. 713-727.
- Liu, D., & Yu, J. (2009). Otsu Method and K-means. *2009 Ninth International Conference on Hybrid Intelligent Systems*. doi: 10.1109/his.2009.74
- Lowe, D. (1999). Object recognition from local scale-invariant features. *Proceedings of the Seventh IEEE International Conference on Computer Vision*. doi: 10.1109/iccv.1999.790410
- Lowe, D. G. (2004). Distinctive Image Features from Scale-Invariant Keypoints. *International Journal of Computer Vision*, 60(2), 91–110. doi: 10.1023/b:visi.0000029664.99615.94
- Massahi, A., Ali, H., Koohifar, F., Baqersad, M., & Mohammadafzali, M. (2018). Investigation of pavement raveling performance using smartphone. *International Journal of Pavement Research and Technology*, 11(6), 553–563. doi: 10.1016/j.ijprt.2017.11.007
- Micheletti, N., Chandler, J. H., & Lane, S. N. (2014). Investigating the geomorphological potential of freely available and accessible structure-from-motion photogrammetry using a smartphone. *Earth Surface Processes and Landforms*, 40(4), 473-486, doi: 10.1002/esp.3648.
- Miradi, M. (2004). Neural network models for analysis and prediction of raveling. *IEEE Conference on Cybernetics and Intelligent Systems*, 2004. doi: 10.1109/iccis.2004.1460766
- Otsu, N. (1979). A Threshold Selection Method from Gray-Level Histograms. *IEEE Transactions on Systems, Man, and Cybernetics*, 9(1), 62–66. doi: 10.1109/tsmc.1979.4310076

- Paterson, W. D. O. (1986). International Roughness Index: Relationship to Other Measures of Roughness and Riding Quality. *65th Annual Meeting of the Transportation Research Board*, (1084), 49–59. Retrieved from <http://worldcat.org/isbn/030904104X>
- Praticò, F., & Vaiana, R. (2015). A study on the relationship between mean texture depth and mean profile depth of asphalt pavements. *Construction and Building Materials*, 101, 72–79. doi: 10.1016/j.conbuildmat.2015.10.021
- Rublee, E., Rabaud, V., Konolige, K., & Bradski, G. (2011). ORB: An efficient alternative to SIFT or SURF. *2011 International Conference on Computer Vision*. doi: 10.1109/iccv.2011.6126544
- Sankur, B. (2004). Survey over image thresholding techniques and quantitative performance evaluation. *Journal of Electronic Imaging*, 13(1), 146. doi: 10.1117/1.1631315
- Seitz, S., Curless, B., Diebel, J., Scharstein, D., & Szeliski, R. (2006). A Comparison and Evaluation of Multi-View Stereo Reconstruction Algorithms. *2006 IEEE Computer Society Conference on Computer Vision and Pattern Recognition - Volume 1 (CVPR06)*. doi: 10.1109/cvpr.2006.19
- Sengoz, B., Topal, A., & Tanyel, S. (2012). Comparison of pavement surface texture determination by sand patch test and 3D laser scanning. *Periodica Polytechnica Civil Engineering*, 56(1), 73. doi: 10.3311/pp.ci.2012-1.08
- Slimane, A. B., Khoudeir, M., Brochard, J., & Do, M.-T. (2008). Characterization of road microtexture by means of image analysis. *Wear*, 264(5-6), 464–468. doi: 10.1016/j.wear.2006.08.045
- Snyder, M. B. (2006). Pavement surface characteristics: a synthesis and guide. *American Concrete Pavement Association*. Retrieved from <http://worldcat.org/isbn/0893122505>
- Ullman, S. (1979). The interpretation of structure from motion. *Proceedings of the Royal Society of London*. 203 (1153), 405–426. doi: 10.1098/rspb.1979.0006
- Wang, W., Yan, X., Huang, H., Chu, X., & Abdel-Aty, M. (2011). Design and verification of a laser based device for pavement macrotexture measurement. *Transportation Research Part C: Emerging Technologies*, 19(4), 682–694. doi: 10.1016/j.trc.2010.12.001
- Westoby, M., Brasington, J., Glasser, N., Hambrey, M., & Reynolds, J. (2012). ‘Structure-from-Motion’ photogrammetry: A low-cost, effective tool for geoscience applications. *Geomorphology*. 179. 300-314. doi: 10.1016/j.geomorph.2012.08.021.
- Yaacob, H., Hassan, N. A., Hainin, M. R., & Rosli, M. F. (2014). Comparison of Sand Patch Test and Multi Laser Profiler in Pavement Surface Measurement. *Jurnal Teknologi*, 70(4). doi: 10.11113/jt.v70.3497